

AD-A193 224

PROCESSING AND PROPERTIES OF ADVANCED ALUMINUM ALLOYS

1/2

(U) VIRGINIA UNIV CHARLOTTEVILLE DEPT OF MATERIALS

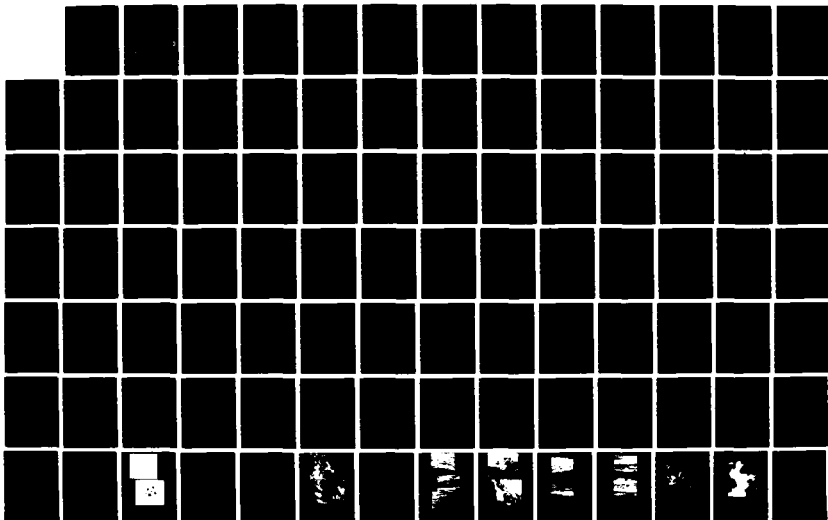
SCIENCE J A MERT ET AL FEB 88 UVA/525670/MS88/101

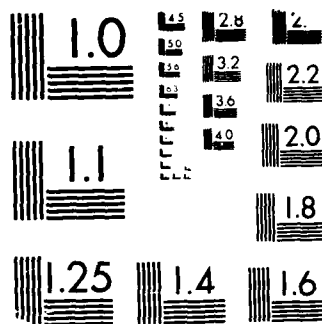
UNCLASSIFIED

AFOSR-TR-88-0285 AFOSR-87-0082

F/G 11/6.1

NL





MICROCOPY RESOLUTION TEST CHART
 NATIONAL BUREAU OF STANDARDS-1963-A

AD-A193 224

An Annual Report
Contract No. AFOSR-87-0082
January 1, 1987 - December 31, 1987

PROCESSING AND PROPERTIES OF ADVANCED
ALUMINUM ALLOYS

Submitted to:

Air Force Office of Scientific Research/NE
Building 410
Bolling Air Force Base
Washington, D.C. 20332

Attention: Dr. Alan H. Rosenstein

Submitted by:

J. A. Wert
Associate Professor

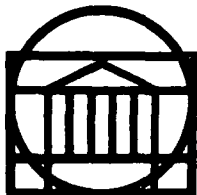
E. A. Starke, Jr.
Earnest Oglesby Professor of
Materials Science and Dean

DTIC FILE COPY

Report No. UVA/525670/MS88/101

February 1988

DTIC
ELECTE
MAR 29 1988
S_aH D



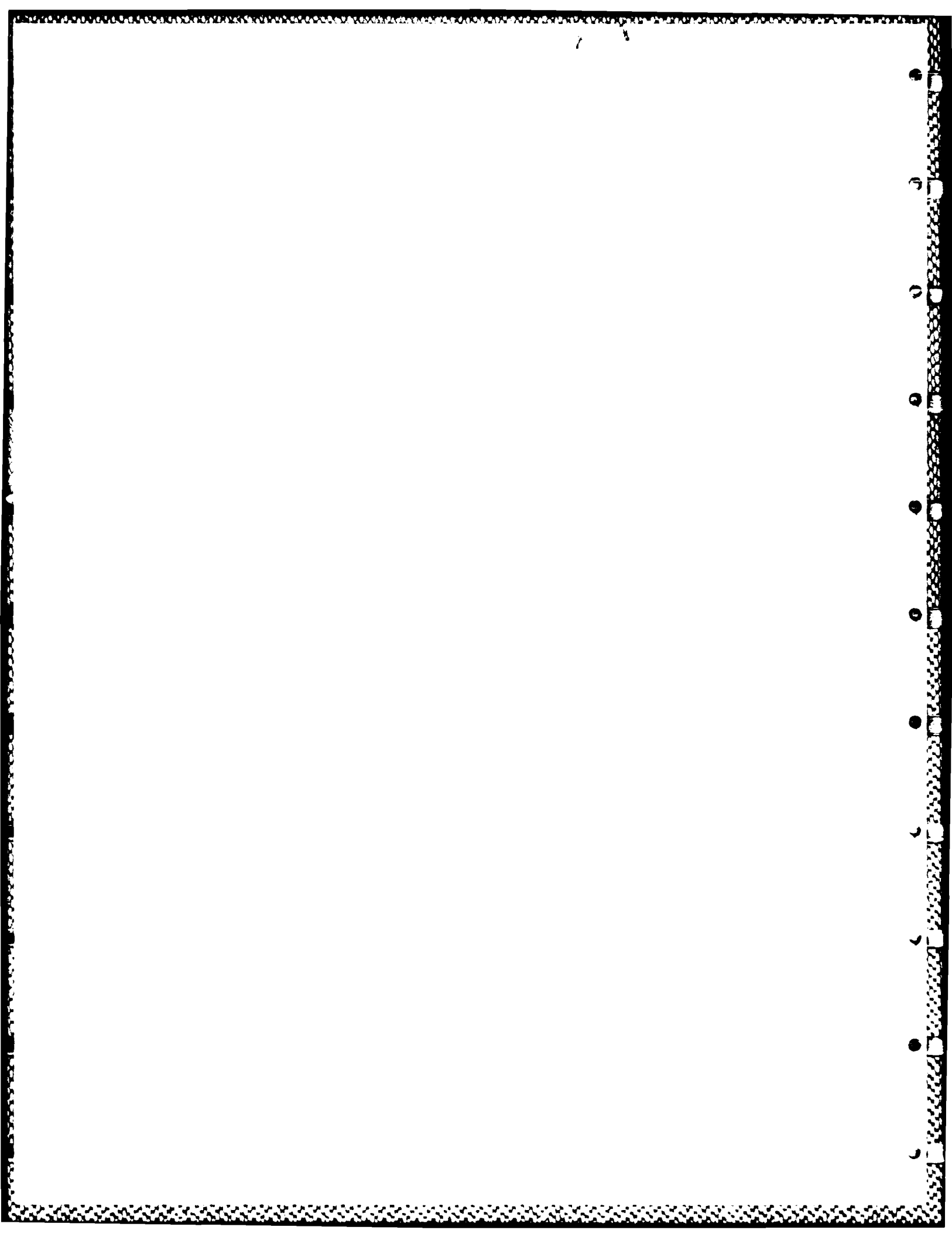
SCHOOL OF ENGINEERING AND
APPLIED SCIENCE

DEPARTMENT OF MATERIALS SCIENCE

DISTRIBUTION STATEMENT A

Approved for public release;
Distribution Unlimited

UNIVERSITY OF VIRGINIA
CHARLOTTESVILLE, VIRGINIA 22901



ANNUAL REPORT
Contract No. AFOSR-87-0082
January 1, 1987 - December 31, 1987

PROCESSING AND PROPERTIES OF
ADVANCED ALUMINUM ALLOYS

Submitted to:

Air Force Office of Scientific Research/NE
Building 410
Bolling Air Force Base
Washington, D.C. 20332

Attention: Alan H. Rosenstein

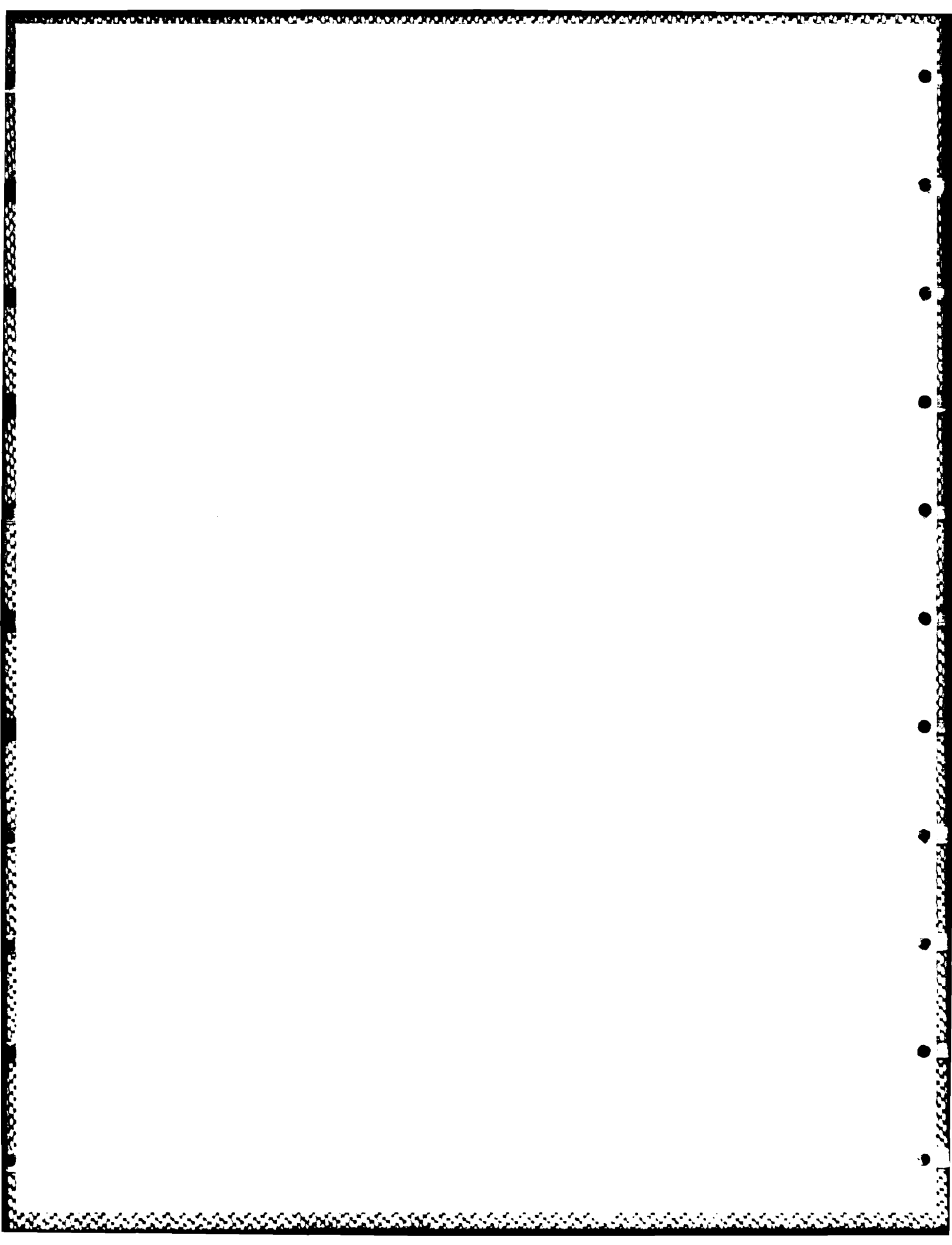
Submitted by:

John A. Wert
Associate Professor

Edgar A. Starke, Jr.
Earnest Oglesby Professor of
Materials Science and Dean

Department of Materials Science
SCHOOL OF ENGINEERING AND APPLIED SCIENCE
UNIVERSITY OF VIRGINIA
CHARLOTTESVILLE, VIRGINIA

Report No. UVA/525670/MS88/101
February 1988



UNCLASSIFIED

SECURITY CLASSIFICATION OF THIS PAGE

REPORT DOCUMENTATION PAGE

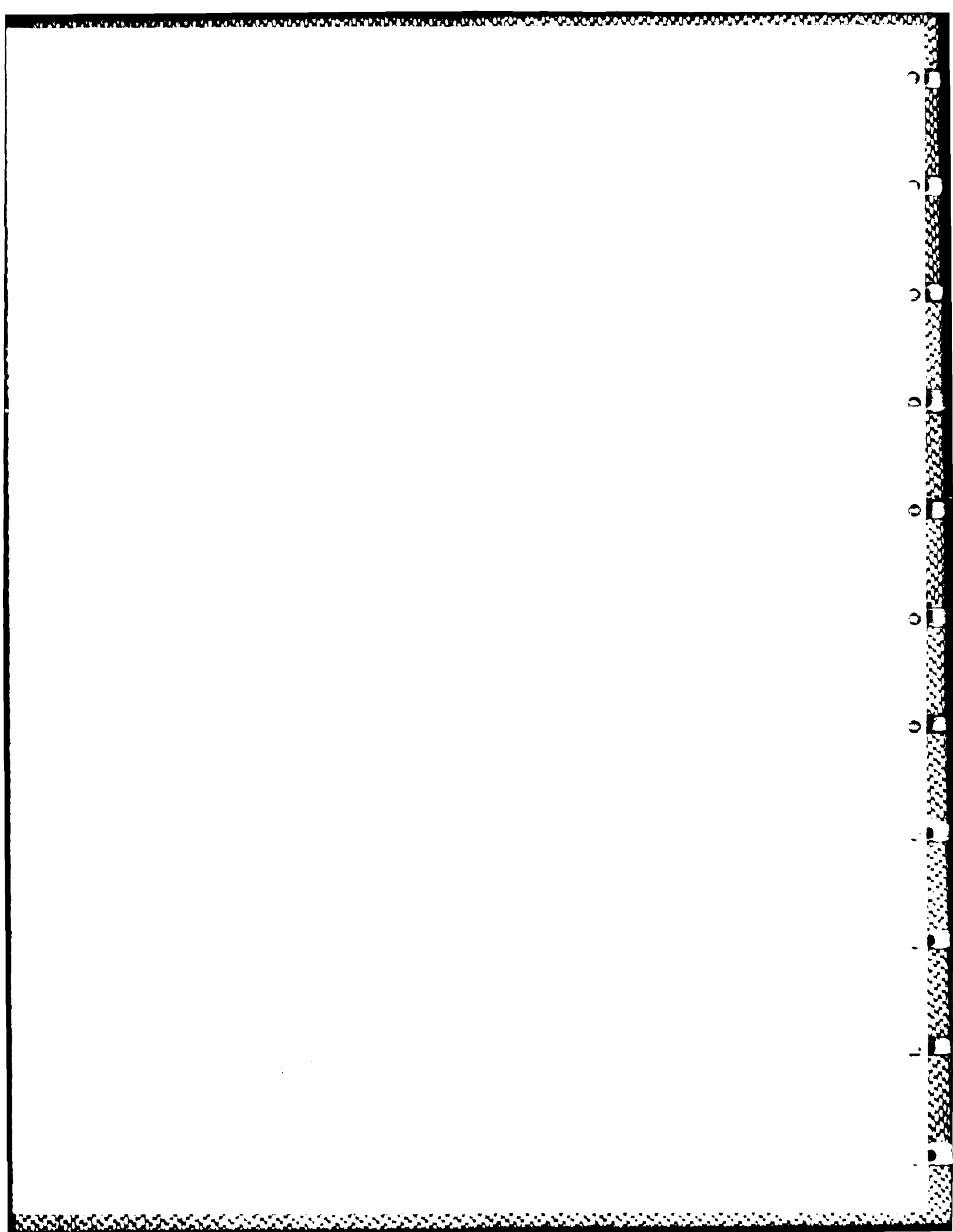
1a. REPORT SECURITY CLASSIFICATION Unclassified		1b. RESTRICTIVE MARKINGS None													
2a. SECURITY CLASSIFICATION AUTHORITY		3. DISTRIBUTION/AVAILABILITY OF REPORT Approved for public release; distribution unlimited.													
2b. DECLASSIFICATION/DOWNGRADING SCHEDULE															
4. PERFORMING ORGANIZATION REPORT NUMBER(S) UVA/525670/MS88/101		5. MONITORING ORGANIZATION REPORT NUMBER(S) AFOSR-TR- 88- 0285													
6a. NAME OF PERFORMING ORGANIZATION University of Virginia Department of Materials Science	6b. OFFICE SYMBOL (If applicable)	7a. NAME OF MONITORING ORGANIZATION Air Force Office of Scientific Research/PKD													
6c. ADDRESS (City, State and ZIP Code) Department of Materials Science Thornton Hall Charlottesville, VA 22901		7b. ADDRESS (City, State and ZIP Code) Building 410 Bolling Air Force Base Washington, D.C. 20332-6448													
8a. NAME OF FUNDING/SPONSORING ORGANIZATION AFOSR/NE	8b. OFFICE SYMBOL (If applicable)	9. PROCUREMENT INSTRUMENT IDENTIFICATION NUMBER AFOSR-87-0082													
8c. ADDRESS (City, State and ZIP Code) Building 410 Bolling Air Force Base Washington, D.C. 20332-6448		10. SOURCE OF FUNDING NOS. <table border="1"><tr><td>PROGRAM ELEMENT NO.</td><td>PROJECT NO.</td><td>TASK NO.</td><td>WORK UNIT NO.</td></tr><tr><td></td><td></td><td></td><td></td></tr></table>		PROGRAM ELEMENT NO.	PROJECT NO.	TASK NO.	WORK UNIT NO.								
PROGRAM ELEMENT NO.	PROJECT NO.	TASK NO.	WORK UNIT NO.												
11. TITLE (Include Security Classification) Processing and Properties of Aluminum Alloys															
12. PERSONAL AUTHOR(S) J.A. Wert and E.A. Starke, Jr.															
13a. TYPE OF REPORT Annual	13b. TIME COVERED FROM 1/1/87 TO 12/31/87	14. DATE OF REPORT (Yr., Mo., Day) 1988 February	15. PAGE COUNT 90												
16. SUPPLEMENTARY NOTATION															
17. COSATI CODES <table border="1"><tr><td>FIELD</td><td>GROUP</td><td>SUB. GR.</td></tr><tr><td></td><td></td><td></td></tr><tr><td></td><td></td><td></td></tr><tr><td></td><td></td><td></td></tr></table>		FIELD	GROUP	SUB. GR.										18. SUBJECT TERMS (Continue on reverse if necessary and identify by block number)	
FIELD	GROUP	SUB. GR.													
19. ABSTRACT (Continue on reverse if necessary and identify by block number) <p>This project has as its focus microstructure control and fracture of advanced aluminum alloys. Our progress report is divided into two major parts: Part I which is concerned with the effect of microstructure on the deformation and fracture of advanced aluminum alloys, and Part II which is concerned with the recovery and recrystallization mechanisms that operate during processing of advanced aluminum alloys.</p> <p>Age hardenable aluminum alloys may undergo relatively brittle intergranular fracture at strains from 2 to 10 times smaller than the strain to fracture for pure aluminum. This phenomenon can be explained in broad terms as follows. Within a grain, an advancing dislocation either bypasses the coherent particles it encounters or cuts through them; cutting reduces the effective size of the obstacle, while bypassing the obstacle effectively enlarges it. If the obstacles are cut, the weakened plane will</p>															
20. DISTRIBUTION/AVAILABILITY OF ABSTRACT UNCLASSIFIED/UNLIMITED <input checked="" type="checkbox"/> SAME AS RPT. <input type="checkbox"/> DTIC USERS <input type="checkbox"/>		21. ABSTRACT SECURITY CLASSIFICATION Unclassified													
22a. NAME OF RESPONSIBLE INDIVIDUAL Alan H. Rosenstein		22b. TELEPHONE NUMBER (Include Area Code) (202) 767-4984	22c. OFFICE SYMBOL												

DD FORM 1473, 83 APR

EDITION OF 1 JAN 73 IS OBSOLETE.

UNCLASSIFIED

SECURITY CLASSIFICATION OF THIS PAGE



continue to slip and deformation will be localized. As a result, dislocations pile up at the grain boundaries at isolated points; the large associated tensions across the grain boundaries open intergranular cracks which propagate without absorbing much energy. A microscopic model of slip in particle reinforced alloys is developed in this section that predicts coarser slip for larger particles for a fixed volume fraction. Coarse slip leads to intergranular fracture in such alloys.

Ductile fracture of the aluminum alloy 2134 has been studied in the under- and overaged conditions for Mn levels ranging from 0.0 to 1.02 wt. percent. The results have been analyzed in terms of areal void density, void growth and void volume fraction of deformed samples. We conclude from this analysis that ductility is controlled by a void link-up process in smooth bars and void growth and void link-up in notched specimens. The results of tensile tests on notched samples also suggest that triaxiality has little effect on the void nucleation rate. Manganese additions have two effects on deformation and fracture: smaller Mn-rich dispersoids homogenize slip thereby delaying void link-up, whereas larger Mn-rich particles increase void density and decrease intervaid spacing. The results of this study indicate that an addition of 0.31 wt. percent Mn produces optimum ductility and fracture toughness in 2131.

The goals of Part II of this investigation are to identify the recovery and recrystallization mechanisms that operate during processing of new aluminum alloys as they relate to material and processing parameters. During the current reporting period, this study has focused on Al-Si-Zr and Al-O-C alloys that contain a high density of dispersoids. These are model materials that exhibit the desired range of microstructural relaxation mechanisms, but avoid complications such as precipitation that are present in technologically-important alloys with similar dispersoid contents. Studies on Al-Si-Zr and Al-O-C alloys have shown that the microstructural evolution during annealing is strongly dependent on the homogeneity of the dispersoid distribution and on the degree of cold deformation. Processing conditions have been found that lead to predominately continuous rather than discontinuous evolution on the cold worked microstructure during annealing. We are currently conducting quantitative analysis of the microstructure to establish the extent of continuous recrystallization as a function of dispersoid content; initial results are reported here. We have also found that concurrent annealing and deforming gives rise to a more rapid continuous recrystallization process. It is believed that continuous recrystallization during concurrent annealing and deformation is responsible for observations of superplasticity at high strain rates; we expect to identify and model these processes during the course of this research.



DTIC TAB		<input checked="" type="checkbox"/>
Unannounced		<input type="checkbox"/>
Justification		
By		
Distribution/		
Availability Codes		
Avail and/or		
Dist	Special	
A-1		

TABLE OF CONTENTS

	Page
PART I. Microstructure Control and Fracture of Advanced Aluminum Alloys	1
1.1 The Effect of Particle Size on the Slip Behavior of Particle Reinforced Alloys. J.M. Duva, M.A. Daeubler, E.A. Starke, Jr., and G. Luetjering . .	1
1.2 The Effect of Aging and Mn Concentration on the Ductile Fracture Behavior of the Aluminum Alloy 2134. J.A. Walsh, K.V. Jata, and E.A. Starke	19
PART II. Processing of Advanced Aluminum Alloys for Structure Control. H. Gudmundsson and J.A. Wert	51

PART I. MICROSTRUCTURE CONTROL AND FRACTURE OF ADVANCED ALUMINUM ALLOYS

1.1. The Effect of Particle Size on the Slip Behavior of Particle Reinforced Alloys.

J.M. Duva, M.A. Daeubler, E.A. Starke, Jr.
and G. Luetjering

Age hardenable aluminum alloys may undergo relatively brittle intergranular fracture at strains from 2 to 10 times smaller than the strain to fracture for pure aluminum. This phenomenon can be explained in broad terms as follows. Within a grain, an advancing dislocation either bypasses the coherent particles it encounters or cuts through them; cutting reduces the effective size of the obstacle, while bypassing the obstacle effectively enlarges it. If the obstacles are cut, the weakened plane will continue to slip and deformation will be localized. As a result, dislocations pile up at the grain boundaries at isolated points; the large associated tensions across the grain boundaries open intergranular cracks which propagate without absorbing much energy. A microscopic model of slip in particle reinforced alloys is developed in this section that predicts coarser slip for larger particles for a fixed volume fraction. Coarse slip leads to intergranular fracture in such alloys.

1. Introduction

Many alloys derive their strength in part from the homogeneous distribution of coherent second phase particles throughout. Accurate predictions of the yield strengths of precipitate hardened alloys are based on the well understood interaction of a dislocation with a particle at the microscopic level. However, precipitate hardened alloys also exhibit low ductility and low fracture toughness, features that also must depend on the presence of the second phase particles. This problem is less well understood.

Age hardenable aluminum alloys in particular may undergo relatively brittle intergranular fracture at strains from 2 to 10 times smaller than the strain to fracture for pure aluminum. This phenomenon can be explained in broad terms as follows. Within a grain, an advancing dislocation either bypasses the coherent particles it encounters or cuts through them; cutting reduces the effective size of the obstacle, while bypassing the obstacle effectively enlarges it. If the obstacles are cut, the weakened plane will continue to slip and deformation will be localized. As a result, dislocations pile up at the grain boundaries at isolated points; the large associated tensions across the grain boundaries open intergranular cracks that propagate without absorbing much energy. Slip becomes more localized as the size of the included particles increases and as the grain size increases. To highlight this idea we briefly review alternative treatments of slip localization in particle hardened alloys.

The resistance stress or strength due to particles in reinforced alloys is given in general by an expression of the form

$$\tau_p = C_p \rho^\alpha r_p^\beta \quad (1)$$

where ρ is the particle volume fraction, r_p is the radius of the particles (assumed to be spherical, equal in size, and small enough to be cut instead of bypassed), and C_p , α , and β are constants that depend on the type of strengthening under consideration and the particular model of the strengthening mechanism used. Sanders and Starke [1] argue that order hardening is the

dominant strengthening mechanism in aluminum-lithium alloys, thus we henceforth restrict our attention to order hardening. Martin [2] estimates the resistance stress due to the particles in this case to be

$$\tau_p = C_p \rho^{1/2} r_p^{1/2}. \quad (2)$$

Here C_p is a function of the energy associated with the creation of antiphase boundary as the particles are cut, the magnitude of the Burgers vector b associated with the dislocation, and the dislocation line tension. Martin models the softening due to the cutting of the particles by using an effective particle radius $r_{eff} = r_p - nb/2$ in the above equation, where n is the number of dislocations that have passed on a given plane. A more precise characterization of the effective size of a cut particle can be used, but the simple expression given above is suitable for the models described herein. When $n = 2r_p/b$ the particle is effectively destroyed. To connect this model of slip softening to localization, Martin reasons that an *indicator* of the tendency toward coarse slip is the degradation rate of the strength with slip:

$$-\frac{\partial \tau_p}{\partial n} = \frac{C_p b \rho^{1/2}}{2(r_p - nb/2)^{1/2}}. \quad (3)$$

This indicator predicts increasingly coarse slip as r_p decreases, a conclusion that is untenable in the limit of vanishingly small particles, and that is contradicted by the experimental evidence of Sanders and Starke [1] and Jata and Starke [3]. These investigators suggest that τ_p itself is an indicator, arguing that if little softening is possible localization cannot result even if the softening occurs rapidly. This indicator predicts coarser slip with increasing particle size. Hornbogen and Zum Gahr [4] combine these ideas in a third alternative:

$$\frac{\tau_p}{\tau_p + \tau_0} \left(\partial \tau_p / \partial n \right) \quad (4)$$

where $\tau_p + \tau_0$ is the yield stress of the material. This indicator is monotonically decreasing in r_p and thus predicts coarser slip for smaller particles, again contrary to observation.

In summary, the indicators proposed are based on a microscopic model of softening and on the intuitive notion that localized slip occurs because a given slip plane is weaker than its neighbors. But the indicators do not give a quantitative connection between slip localization and alloy properties. The task of constructing a quantitative microscopic model of slip is taken up in the following section.

2. A Model of Slip Localization

The indicators discussed above are all based on a simple and accurate model of the strength due to the presence of second phase particles and the degradation of that strength with slip. We augment this basic model by also considering the strengthening effect of dislocation pile-ups. Whether or not a particular slip plane undergoes a net weakening with slip will depend on the relative intensities of these two competing mechanisms, which in turn depend on material parameters and the current distribution of slip in the material.

The model we propose does not account for many subtle factors, including interaction between slip planes, the nature of dislocation sources present, and the full variety of possible hardening and softening mechanisms. In the following we introduce an indicator of slip localization that agrees qualitatively with observations and, through rudimentary kinematic arguments, we derive an expression for the slip band spacing.

2.1. The Slip Intensity Indicator

We assume that if slip weakens a particular plane then slip will continue on that plane until it regains the strength it had when softening commenced. During this process hardening does not begin until the strength due to the particles has been completely exhausted, thus a large amount of *local* slip can occur in this instance.

We take the number of dislocations N that pass on a typical slip plane from the time deformation begins until local slip ends to be an indicator of slip localization. The larger the slip inten-

sity as measured by N , the coarser the deformation expected. The direct connection between N and the simple intergranular fracture mechanism discussed above makes N a convenient indicator. The stress concentration at the grain boundary associated with the pile-up of N dislocations is $\tau^* = N\tau_s$, where τ_s is the resolved shear stress. If τ^* exceeds the crack nucleation stress at the grain boundary, intergranular fracture starts.

By considering the strengthening effects of both the second phase particles and the dislocation pile-ups at the grain boundaries, the strength of a particular slip plane can be written as

$$\tau = \tau_o + C_P \rho^{1/2} (r_P - nb/2)^{1/2} + C_B nb/r_G \quad (5)$$

where r_G is the grain radius and C_B is a constant that depends on the elastic properties of the bulk material. The third term on the right can be regarded as the backstress at the grain center due to a superdislocation (with Burgers' vector nb) at the grain boundary or as the backstress at the tail end of a pileup of length r_G containing n dislocations. With either interpretation it is an approximate measure of the inhibiting effect of the pileup on subsequent slip. An additional term representing the strength due to pile-ups on other slip planes is not included. Although the contribution from this term is of the order of the last term on the right, it is not a function of n and does not affect the calculation of N . It may be thought of as contributing to τ_o , which represents the background strength of the material.

We have assumed that if slip weakens a particular plane that slip will continue on that plane until it regains the strength it had when the softening commenced. Softening, that is the degradation of strength with increasing n , is indicated by the derivative of τ with respect to n being less than or equal to zero. Note that softening must occur for some value of n according to equation (5) because the contribution to $\partial\tau/\partial n$ from the particle strengthening term is negative and grows infinitely large as n approaches $2r_P/b$. The slip intensity N is calculated below for the two possible regimes: (I) if $\partial\tau/\partial n \leq 0$ prior to deformation then softening occurs immediately; (II) if $\partial\tau/\partial n > 0$ prior to deformation then hardening will occur initially and softening will occur only

after some slip has taken place.

(I) *Softening occurs initially*

Softening occurs initially if $\partial\tau/\partial n \leq 0$ and continues as long as this inequality holds. Written explicitly and solved for r_p the inequality is

$$r_p \leq \frac{nb}{2} + \rho r_G^2 \left[\frac{C_p}{4C_B} \right]^2. \quad (6)$$

Given the grain size, the particle volume fraction and the material properties, equation (6) is satisfied only for sufficiently small particle radius. In this instance slip will continue until τ again reaches its initial value, thus

$$N = \rho^{1/2} r_p^{1/2} r_G \frac{C_p}{C_B b}. \quad (7)$$

Although we are primarily interested in the dependence of N on r_p , equation (7) also gives the dependence of N on r_G and ρ in the case that softening occurs initially. The slip intensity N increases with the square root of both the particle volume fraction and the particle radius and increases linearly with the grain radius.

(II) *Hardening occurs initially*

Hardening occurs initially if $\partial\tau/\partial n > 0$ and continues as long as

$$r_p > \frac{nb}{2} + \rho r_G^2 \left[\frac{C_p}{4C_B} \right]^2. \quad (8)$$

holds. Those planes initially more susceptible to slip than others, because they contain dislocation sources or other stress concentrators for instance, will share the deformation until the first one begins to soften. This occurs when the maximum strength has been reached after

$$n_1 = \frac{2}{b} r_p - \frac{2}{b} \rho r_G^2 \left[\frac{C_p}{4C_B} \right]^2 \quad (9)$$

dislocations have passed. The calculation of the value of the maximum strength on a particular

plane is complicated by the presence of pile-ups on neighboring planes. However, once weakening has started, slip will continue until the strength returns to this maximum value, thus

$$N = \frac{2}{b} r_p + \frac{2}{b} \rho r_G^2 \left(\frac{C_p}{4C_B} \right)^2. \quad (10)$$

Again, equation (10) gives the dependence of N on ρ and r_G as well as the dependence of N on r_p in the case that hardening occurs initially. The slip intensity N increases linearly with r_p and ρ and increases as the square of r_G .

2.2. Slip Band Spacing

Consider a cubic grain with edge length $2r_G$ and suppose the grain is subjected to a shear strain γ . We assume that γ , although small, is much larger than r_p/r_G . (In aluminum-lithium alloys this latter ratio is typically 10^{-4} .) This assumption insures that enough slip occurs so that the particles are completely sheared on many different planes. We also neglect elastic strains. Then

$$s = Nb/\gamma \quad (11)$$

where s is the band spacing from center to center. See Figure 1. Terlinde and Luetjering [5] present a more carefully derived relation that gives the same proportionality between s and N under the assumptions stated above.

3. Discussion of the Present Model

It has been shown that for a given strain γ the slip band spacing is directly proportional to the slip intensity N . The influence of the variable parameters r_p , r_G and ρ on N , as expressed in equations (7) and (10), will be discussed for each of the variables separately.

Influence of Particle Radius

For constant values of ρ and r_G and sufficiently small values of r_p initial softening occurs (regime I), as illustrated in Figure 2. Alternatively, if r_p is sufficiently large, again for constant values of ρ and r_G , initial hardening occurs (regime II), as illustrated in Figure 3. The dependence

of slip intensity N on particle radius is depicted schematically in Figure 4, and the separation of regimes I and II is indicated there. For sufficiently small particle radius (regime I), N is proportional to $r_p^{1/2}$, whereas for sufficiently large particle radius (regime II) N increases linearly with r_p . We emphasize that in either case slip localization is enhanced as the particle radius increases. Increasing N also means increasing the slip band spacing, according to equation (11).

Influence of Grain Size

For constant values of ρ and r_p and sufficiently small values of r_G initial hardening takes place (regime II), as illustrated in Figure 5. If r_G is sufficiently large, again for constant values of ρ and r_p , initial softening (regime I) takes place, as illustrated in Figure 2. The slip intensity N increases as the square of the grain radius for sufficiently small grains (regime II) and increases linearly with grain size for sufficiently large grains (regime I). The dependence of slip intensity N on grain radius is depicted schematically in Figure 6, and the separation of regimes I and II is indicated there.

Influence of Particle Volume Fraction

For practical applications the variation in particle volume fraction is only of subordinate importance but shall be discussed for completeness. For sufficiently small values of ρ and constant values of r_G and r_p initial hardening occurs (regime II), as depicted in Figure 5. For sufficiently large values of ρ and constant values of r_G and r_p initial softening occurs (regime I), as shown in Figure 7. The dependence of the slip intensity N on particle volume fraction is depicted schematically in Figure 8, and the particle volume fraction separating regimes I and II is indicated. The slip intensity N is proportional to the $\rho^{1/2}$ for sufficiently large particle volume fractions (regime I) and is proportional to ρ for sufficiently small particle volume fractions (regime II).

4. Conclusions

A microscopic model of slip in particle reinforced alloys has been proposed that predicts coarser slip for larger particles for a fixed particle volume fraction and grain size. Simple kinematic arguments also have been proposed that yield estimates of the slip band spacing in such alloys and their dependence on particle size, particle volume fraction and grain size. Data presented by Jata and Starke [3] support the contentions above in as much as the trends in the data for band spacing and band width are consistent with expectations based on the above analysis. This model predicts decreasing strains to fracture with increasing particle size. Terlinde and Luetjering [5] have produced a model of tensile fracture for a Ti-Al alloy based on the localization of slip within grains and the associated stress concentrations at the grain boundaries due to pile-ups. Their results too are consistent with the above analysis.

Bibliography

1. Sanders, T.H. Jr. and E.A. Starke Jr., "The Effect of Slip Distribution on the Monotonic and Cyclic Ductility of Al-Li Binary Alloys," *Acta Met*, **30**, p 927, 1982.
2. Martin, J.W., "Micromechanisms in Particle-Hardened Alloys," Cambridge University Press, 1980.
3. Jata, K.V. and E.A. Starke Jr., "Fatigue Crack Growth and Fracture Toughness Behavior," *Met Trans A*, **17A**, p 1011, 1986.
4. Hornbogen, E. and K.H. Zum Gahr, "Distribution of Plastic Strain in Alloys Containing Small Particles," *Metallography*, **8**, p 181, 1975.
5. Terlinde G. and G. Luetjering, "Influence of Grain Size and Age Hardening on Dislocation Pile-ups and Tensile Fracture for a Ti-Al Alloy," *Met Trans A*, **13A**, p 1283, 1982.

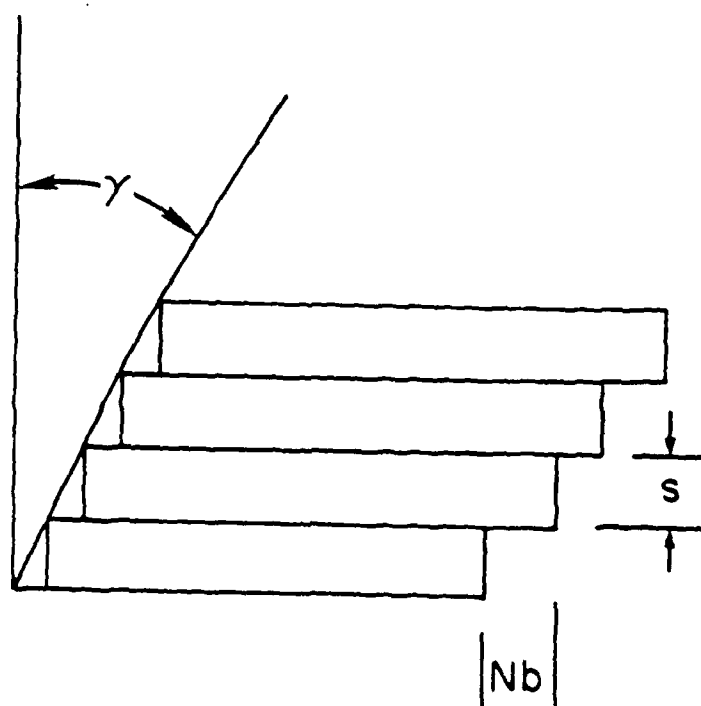


Figure 1. A kinematic model relating the slip intensity, λ , to the imposed strain γ and the slip band spacing s .

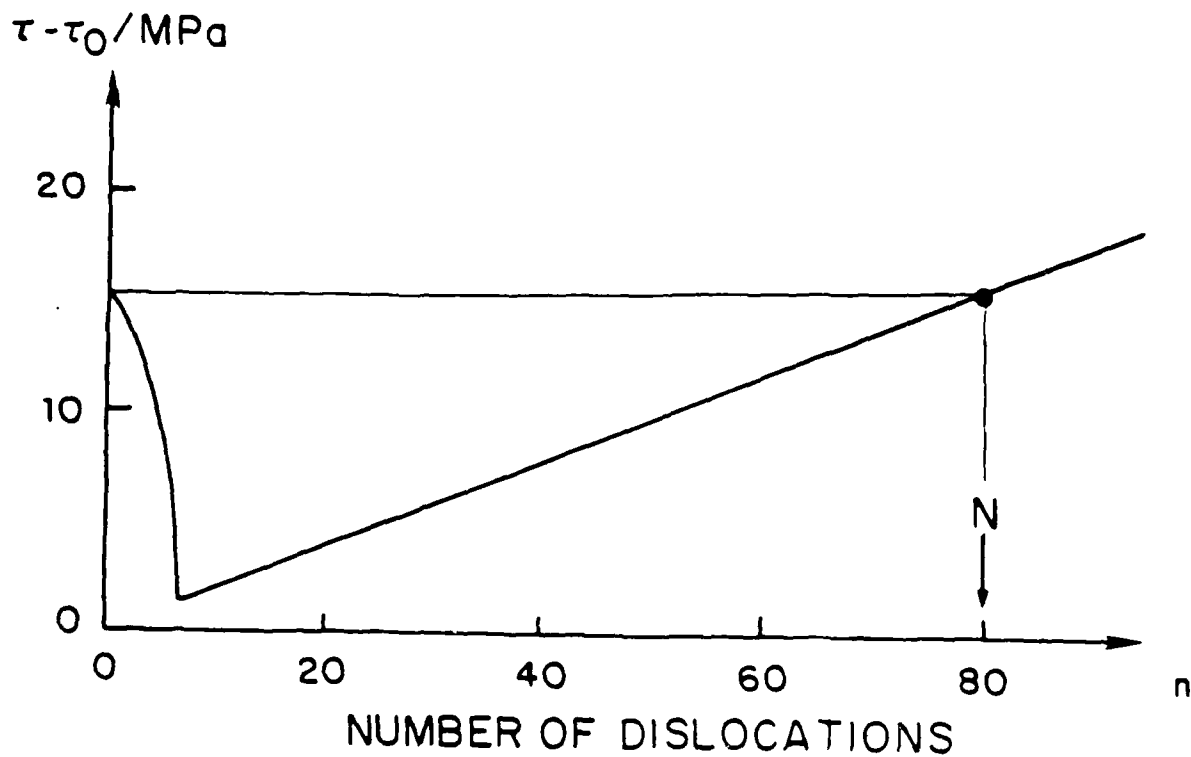


Figure 2. Initial softening (regime II). Strength vs. n for Ti-6Al-4V, $\sigma_0 = 100$ MPa, $P = 1.1$, and $\sigma_3 = 100$ MPa.

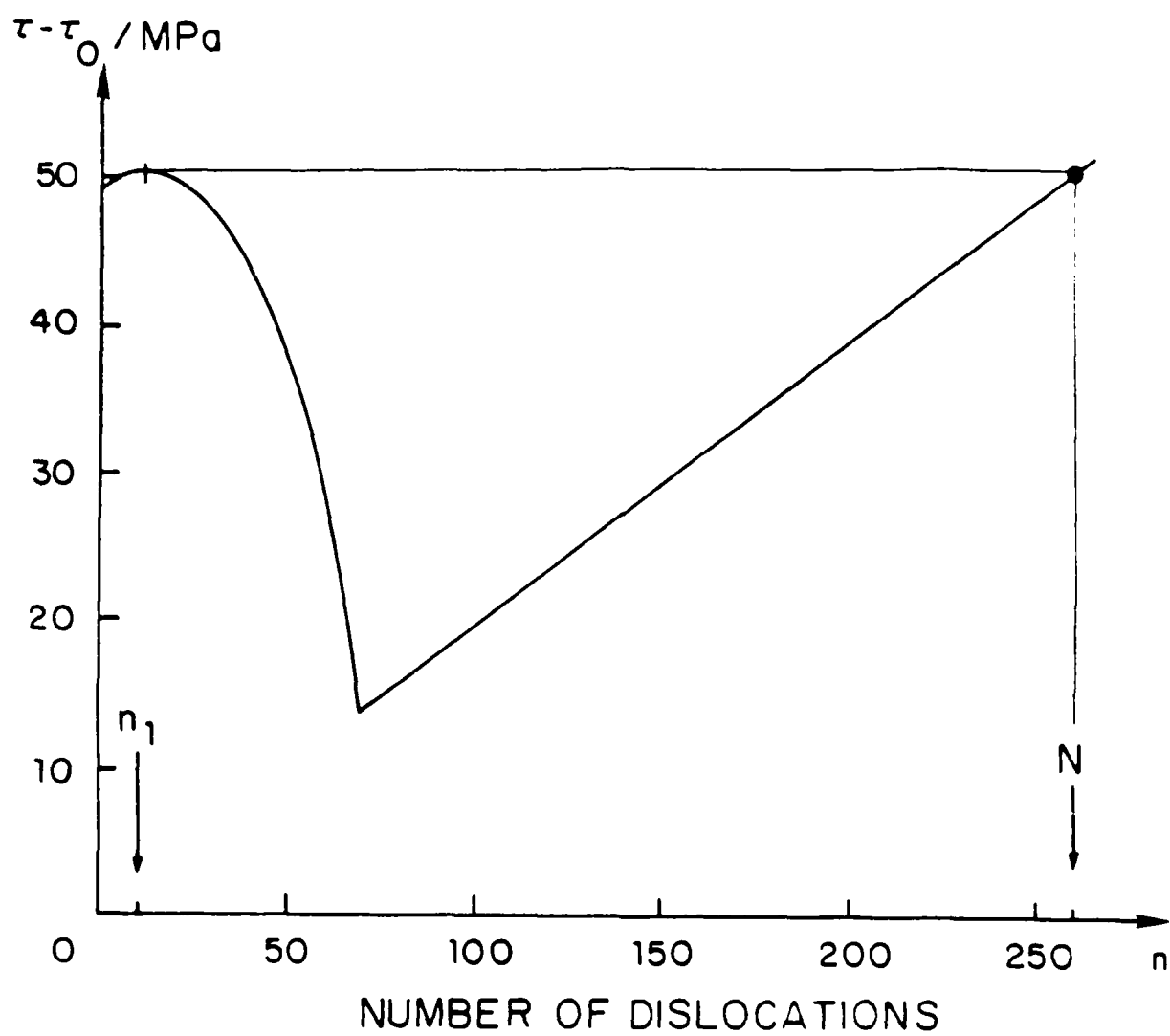


Figure 7. Cyclic hardening response of Ti-6Al-4V. Strength values for $\tau_0 = 100$ MPa, $P = 0.1$, and $\rho_0 = 1 \times 10^8 \text{ m}^{-2}$.

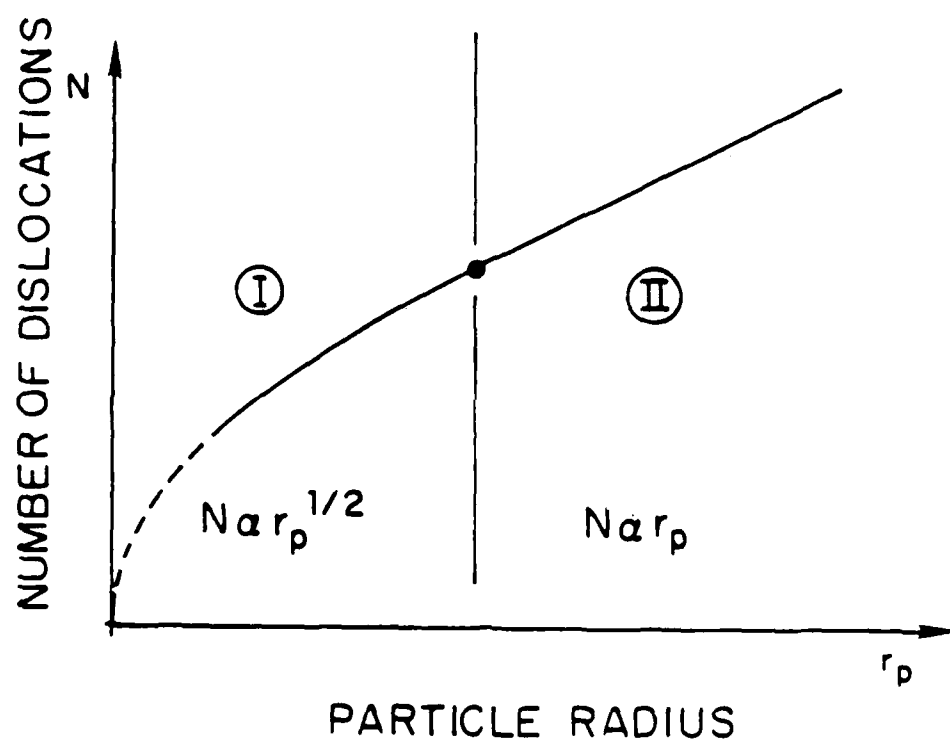


Figure 4. Diffraction intensity, I , vs. particle radius r_p .

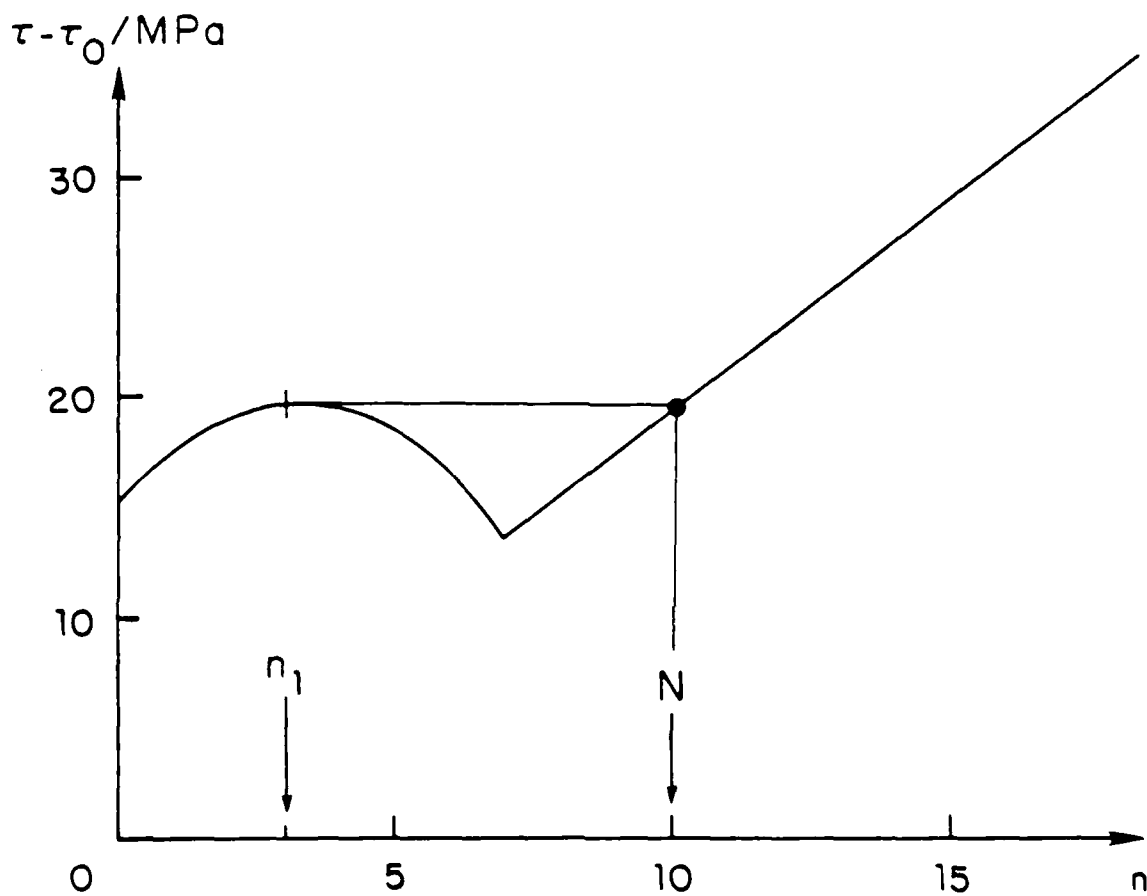


Figure 3. Cyclic hardening (baseline 1). Strength vs. n for $\tau_0 = 47$ MPa, $n_0 = 10$, $P = 1$, and $n_1 = 3.5$.

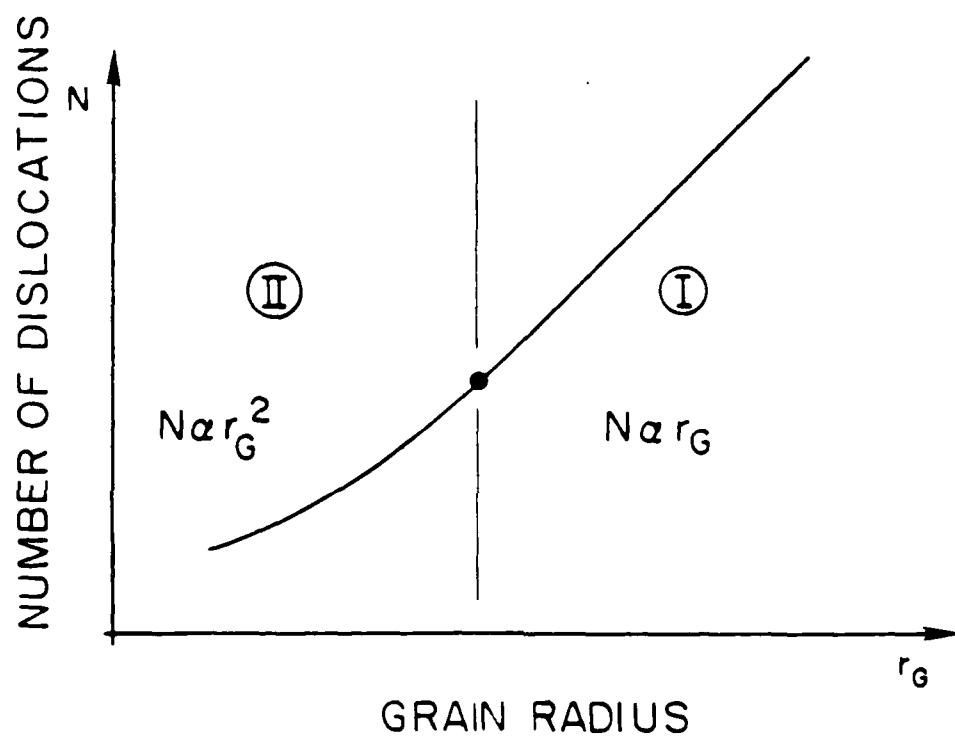


Figure 6. Diff. Intensity, I , vs. grain radius r_G .

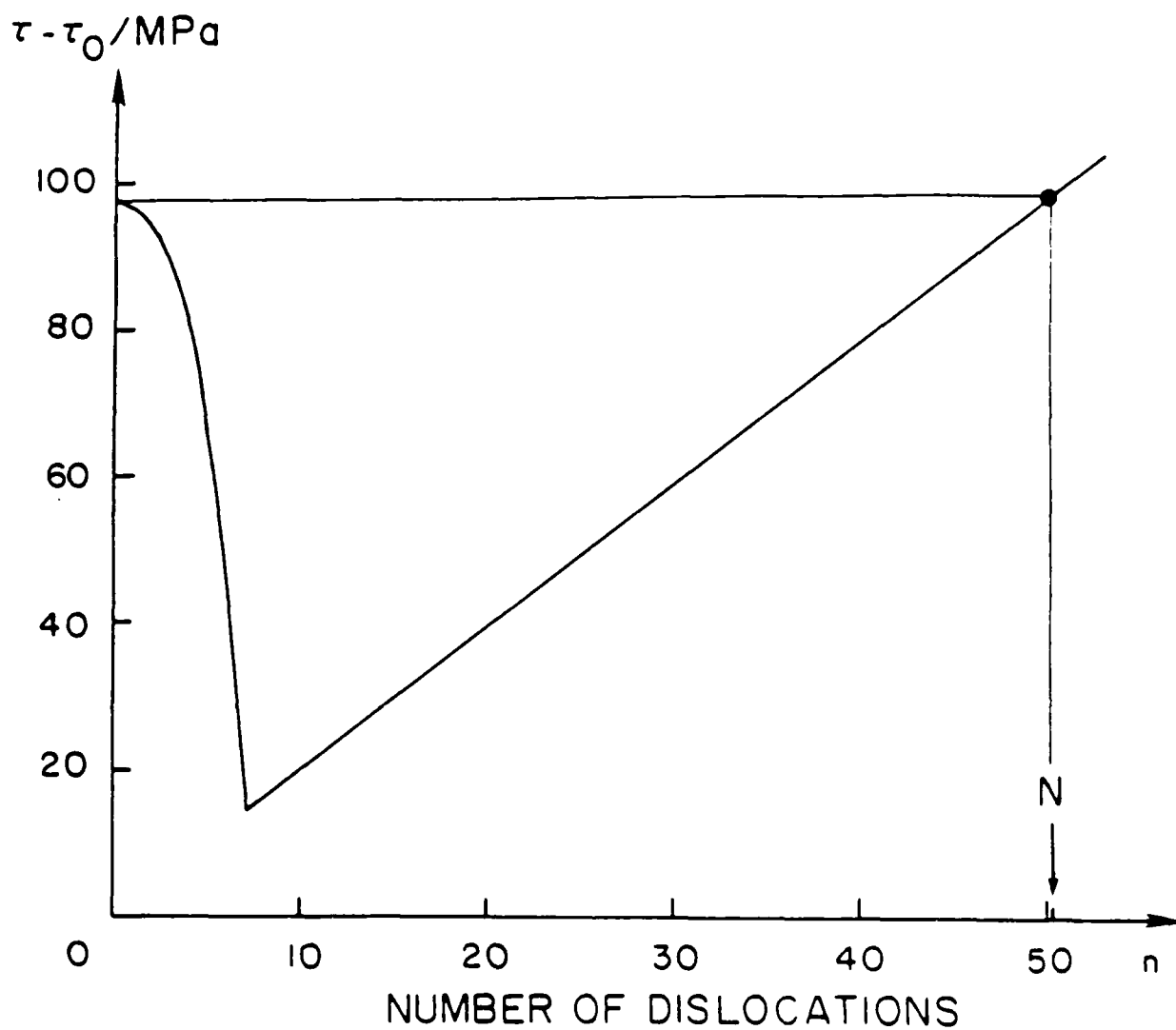


Figure 7. Initial softening regime. Strength vs. dislocation density for Ti-6Al-4V, $n_0 = 10^8$, $\rho = 1.4$, and $n_0 = 10^8$.

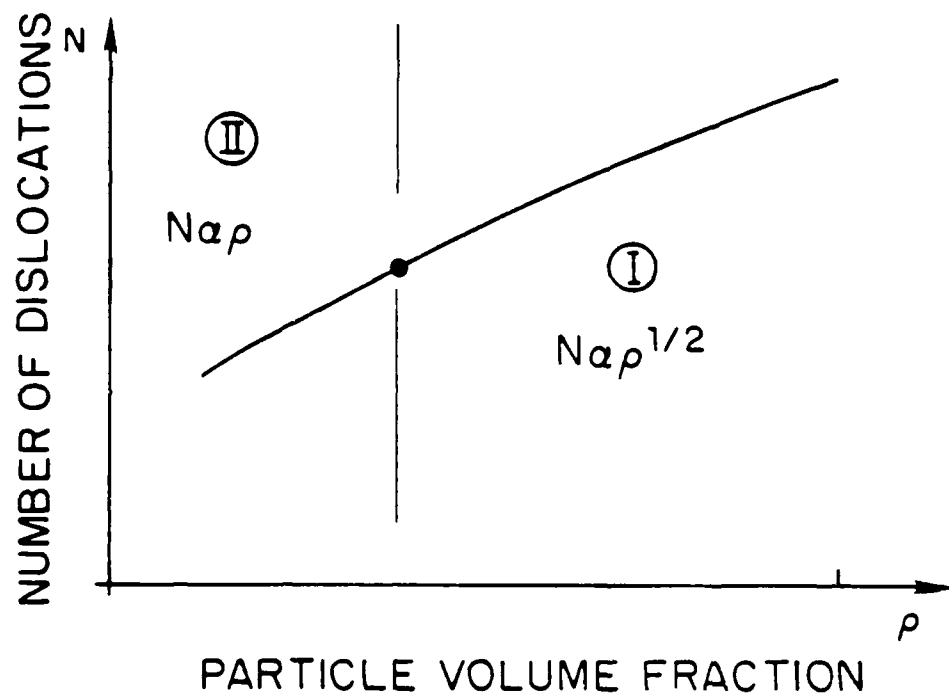


Figure 3. Slip intensity N vs. particle volume fraction ρ .

PART I. MICROSTRUCTURE CONTROL AND FRACTURE OF ADVANCED
ALUMINUM ALLOYS

1.2. The Effect of Aging and Mn Concentration
on the Ductile Fracture Behavior of the
Aluminum Alloy 2134.

J.A. Walsh, K.V. Jata and E.A. Starke, Jr.

Ductile fracture of the aluminum alloy 2134 has been studied in the under- and overaged conditions for Mn levels ranging from 0.0 to 1.02 wt. percent. The results have been analyzed in terms of areal void density, void growth and void volume fraction of deformed samples. We conclude from this analysis that ductility is controlled by a void link-up process in smooth bars and void growth and void link-up in notched specimens. The results of tensile tests on notched samples also suggest that triaxiality has little effect on the void nucleation rate. Manganese additions have two effects on deformation and fracture: smaller Mn-rich dispersoids homogenize slip thereby delaying void link-up, whereas larger Mn-rich particles increase void density and decrease intervoid spacing. The results of this study indicate that an addition of 0.31 wt. percent Mn produces optimum ductility and fracture toughness in 2131.

1. Introduction

Ductile fracture involving void nucleation, growth and coalescence is commonly encountered in most alloys. Aluminum alloys, e.g., 2124 Al alloy [1,2], which contain incoherent second phase particles such as Fe and Si constituents and Mn dispersoids fracture by this mechanism. In order to relate ductility to microstructure, analysis of ductile fracture has commonly been performed on deformed and sectioned tensile specimens. Metallographic analysis of such samples can give information on void nucleation, growth and coalescence, all of which are involved in ductile fracture. Using these methods, Argon et al. [3-5] have shown that a large volume fraction of large particles can result in a lower nucleation strain for void formation than necessary when a small volume fraction of small particles is present. The stress state [6,7] can also have a significant effect on the ductility and hence on the ductile fracture process. Although a hydrostatic stress almost always increases the void growth rate [8], its effect on the nucleation strain is not clear [3-5,9]. In aluminum alloys, the slip mode can also have a significant effect on the ductility and the fracture process. The effect of slip mode on fracture strain for materials having the same yield stress has not been studied systematically. Psioda et al. [2] studied maraging steels and suggest that coarse planar slip can lead to a larger number of voids than when finer planar slip predominates, but deformation changes were accompanied by changes in yield strength.

The objective of the present research is to examine the effect of variations in the volume fraction of second phase

particles (other than strengthening phases), slip mode, and stress state on the ductile fracture of 2134 type alloys containing different Mn levels.

2. Materials

The materials used in this study were four Al-Cu-Mg-Zr alloys with traces of Si, Fe and Ti, and varying amounts of Mn additions. The actual chemical compositions of these 2134 type alloys are shown in Table 1. They are similar in composition to 2124 (Aluminum Association designation) with the addition of Zr as the dispersoid-forming element.

The alloys were obtained from the Reynolds Metals Company in the form of 20.32 mm thick plates. These were hot rolled between 371^o-471^oC and then solutionized at 493^oC for 1.5 hours, water quenched and stretched 2.5% to produce the T351 temper. All alloys were aged for 2 to 4 hours at 190^oC to obtain an underaged condition and for 24 hours to obtain an overaged condition.

Grain size measurements were determined using an average value from the rolling, longitudinal, and short transverse planes. The equations and method used to calculate the grain size were in accordance with ASTM specifications E112. The volume fraction, size and spacing of the large constituent phases were also determined from optical micrographs. The equivalent diameter D_{ef} and the equivalent grain size number G_{eg} , Table 2, were approximately the same for all four alloys and, therefore, grain size effects were not important in this study.

The size and spacing of the large Al_2Cu , Al_2CuMg , and $Al_{20}Cu_2Mn_3$ constituent phases are given in Table 3. The

distribution as measured at 300 X is shown in Table 3, where V_v is the volume fraction, N_L the lineal fraction, λ the mean free distance, and σ the mean particle spacing of the particles. Tensile testing was performed on smooth and notched specimens at a strain rate of $1 \cdot 10^{-3}$ /sec. The dimensions of the notched specimens are shown in Table 4. In this table R_0 is the radius of curvature of the notch and a_0 is the minimum radius of the sample. σ_T is the triaxial or mean stress and Y is the flow stress.

The volume fraction of voids present in deformed tensile samples was obtained through picnometer measurements and the maximum void size and voids/mm² were obtained from SEM micrographs. The room temperature mechanical properties of all four alloys are given in Table 5.

3.1 Damage from Void Nucleation and Growth in Smooth Tensile Specimens

Picnometer measurements of void volume fractions, V_f , of deformed specimens reflect the combined damage due to void nucleation, growth and coalescence. V_f for different Mn levels is shown in Figure 1(a)-(d) for under- and overaged conditions. The increase in V_f for both aged conditions follow similar trends as a function of deformation. Additions of Mn produce an increase in the void volume fraction, particularly in the overaged condition and in alloys #3 and #4, Figures 2 and 3. Alloy #4 shows a higher void volume fraction prior to fracture for both aged conditions than the other three alloys; alloy #3 shows the next highest void volume fraction and alloys #1 and #2 show

only small differences in void volume fraction from each other and less than alloy #3. The damage accumulation rate with respect to strain (slope of the curves at every strain level) is substantially higher for alloy #4, which contains a significantly higher volume fraction of closely spaced large particles when compared to the other three alloys, Table 3. This higher damage accumulation rate results in a considerable decrease in tensile fracture strain in comparison to the other alloys. Alloys #1, #2 and #3, on the other hand, show somewhat similar damage accumulation rates except in the overaged condition. The critical void volume fraction, V_{fc} , i.e., the total damage content at fracture (as indicated by X in Figures 1 and 2) for alloys #2, #3 and #4 is higher than that for alloy #1. This effect is more pronounced for the overaged condition. In alloy #4, inspite of highest rate of damage accumulation and lowest strain to fracture, the critical void volume fraction at fracture is higher than the other alloy variants in both under- and overaged conditions. The high value of V_{fc} indicates that the final link-up of voids is delayed, which may be attributed to a more homogeneous strain distribution in this alloy. Alloy #2 for both aging conditions has a higher V_{fc} than determined for alloy #1. This is due to a higher degree of homogeneously distributed strain and, therefore, a delayed link-up of voids. Unlike alloy #4, alloy #2 does not exhibit a high rate of damage accumulation, and this results in an increased ductility. Alloy #3 shows a slightly smaller V_{fc} than #2 which is most likely associated with a smaller interparticle spacing combined with approximately

the same degree of slip homogenization.

3.2 Damage from Nucleation of Voids in Smooth Tensile Specimens

The number of voids per mm^2 (areal void density) was obtained as a function of strain on deformed specimens from SEM's at a magnification at 1000 X. The lowest strain examined was 0.02. Data was taken until the standard deviation remained constant within 5% to assure statistical confidence. The results are shown in Figures 4 (a) and (b), for the under- and overaged conditions for the alloy variants examined. These results indicate the increase in the areal void density to be linear with deformation and, furthermore, that voids are being continually nucleated during deformation. The slopes of the lines suggest that the void nucleation rate is much higher for alloy #4 for both aging conditions, Table 6. In the overaged condition alloy #4 exhibits two nucleation rates: a lower nucleation rate at low strain levels and a higher nucleation rate at higher strains. Alloy #4's high nucleation rates are most likely due to its greater volume fraction and closer spacing of larger particles, which provide multiple nucleation sites. These microstructural features interact with the stress/strain fields resulting in a higher local stress/strain at the large particle/matrix interface, thus enabling the critical stress/strain for void nucleation to be attained at lower applied strains [3-4]. The under- and overaged alloys show relatively small differences for #3 and #4, but the #1 and #2 underaged alloys display greater rates of nucleation than do the overaged alloys. Thus a change in the deformation mode from localized slip in the underaged

condition to dispersed slip in the overaged condition [10], affects the #1 (0% Mn) and #2 (0.3% Mn) alloys more than it does the high Mn containing alloys. The higher degree of homogeneous slip in the overaged alloys reduces the likelihood of the critical stress/strain concentration to cause particle fracture or decohesion in #1 and #2. The underaged condition, on the other hand, provides local increases in stress/strain due to localized slip. The increase in the rate of nucleation of voids and the number of voids/mm² is in fact observed to be greatest for the #1 underaged alloy which does not contain any Mn and exhibits the highest degree of localized slip. The incidence of particle cracking due to intense planar slip and low particle cracking stress has previously been observed in an aluminum alloy [11]. Both Ashby [12] and Argon [3-5] suggest that the mechanism of particle cracking due to increased planar slip is valid due to an increased probability of a longer particle interfering with planar slip as compared to a smaller particle. The addition of Mn in alloys #3 and #4 (0.6% and 1.02%) not only increases the dispersoid population but also homogenizes slip even in the underaged condition. Hence, the under- and overaged alloys show a similar nucleation behavior; however, due to their larger volume fractions of large particles, alloys #3 and #4 have larger areal void densities than either alloy #1 or #2.

3.3. Damage from void growth

The average maximum void size, L_{max} , measured as a function of strain along the stress axis is shown in Figures 5 and 6. Growth of these voids occurred primarily parallel to the stress

axis. In the transverse direction void growth was not noticeable until very high triaxialities were reached -- approaching the fracture strain in the smooth specimens. Therefore, L_{\max} was measured as a function of strain only along the stress axis. In both aging conditions, alloy #4 showed a much larger void size than the other alloys at comparable strain levels. The largest void size was also attained at a lower strain level than observed for the other alloys as was the rate of void growth. In the overaged condition, the addition of Mn resulted in a more rapid increase in the average maximum void size with deformation. This trend was also observed for alloys #2, 3 and 4 in the underaged condition. However, alloy #1 had voids larger than either #2 or #3 at equivalent strains. A comparison of the relative size of voids in the underaged condition to those in the overaged condition reveals that the underaged alloys produce larger voids and smaller fracture strains. Therefore, homogeneous deformation or slip dispersal due to overaging reduces local deformation and thus reduces void growth. These results clearly show that void sheet formation which occurs prior to final fracture takes place at lower strains in the underaged alloys, illustrating the adverse effects of localized slip. The differences in the void growth rates between the #1, #2 and #3 overaged alloys do not appear to be significant, Table 7.

3.4. Triaxiality Effects

The effect of triaxiality on ductile fracture was studied only in alloy #3 in the under- and overaged conditions. Table 8 shows the conditions of triaxial specimens and corresponding

fracture strains. The effect of triaxiality on fracture strain for the under- and overaged alloys is shown in Figure 7. σ_T/Y was used as a measure of triaxiality as determined from Bridgeman's equation [13]. As the triaxiality increases, the strain to fracture drops more rapidly in the overaged alloys than in the underaged. In fact at the largest triaxiality (T_5) the overaged alloy has less than half of the fracture ductility of the underaged alloy: 0.053 as compared to 0.115. The reduction in ductility has also been noted previously by Ritchie et al. [14] in pressure vessel steel.

The void volume fraction or damage accumulation was determined on samples with triaxiality ranging from T_0 - T_4 . In the T_5 condition V_f could not be measured due to a small deformed volume. As shown in Figures 8 and 9, increasing triaxiality results in a large increase in damage at any strain; however, the critical void volume fractions remain constant until T_3 is approached. At T_4 there is a large drop in the critical void volume fraction together with a large reduction in ductility. A similar result is observed for the overaged alloy. In addition, the overaged alloy exhibits greater damage than the underaged alloy for the T_4 condition. The higher damage accumulation in the overaged alloy gives rise to a lower fracture strain, Figure 10.

The effect of triaxiality on the areal void density, Figure 11 (a) and (b), before the specimens fracture appears to be insignificant. The rate of void nucleation for the T_4 overaged alloy, however, is only slightly larger than that observed for the other triaxiality conditions, Table 9. The growth of voids did change significantly with triaxiality for both aging

conditions. The maximum void size as a function of strain is shown in Figures 12 and 13 for the T_0 and T_4 conditions. Since the voids/mm² parameter did not change sufficiently with triaxiality, it is the void growth that contributes to the increased damage associated with triaxiality.

4. Discussion

The ductile fracture process of the present alloys is one of void nucleation, growth and coalescence. Void formation was observed to occur either through the separation of the interface between equiaxed Al_2Cu/Al_2CuMg particles and the matrix or the brittle cracking of nonequiaxed $Al_{20}Cu_2Mn_3$ particles. The fracture surfaces, with the exception of the underaged alloy #1, exhibited a dimpled rupture type of failure. Some shear fracture, in addition to dimpled rupture, was observed for alloy #1, which does not contain any Mn. The shear fracture was associated with slip localization between the large constituent particles. This fracture mode was reduced by the addition of Mn when the alloy was overaged. Since shear fracture involves a minimum amount of void nucleation and growth, a low void content should be expected. This is clearly reflected in the void volume fraction measurements, Figure 2. In fact, the #1 UA alloy exhibited the lowest critical void volume fraction (which contains damage from nucleation, growth and coalescence) of all the alloys inspite of a higher ductility than either alloy #3 or #4, both of which failed by a total microvoid coalescence type of failure.

The ductility in smooth specimens of all the overaged alloys

is higher than the underaged variants with correspondingly higher critical void volume fractions. Since the volume fraction and spacing of large void nucleating particles should not change with aging, the differences in the critical void volume fractions should arise either from a difference in the deformation mode, or a difference in the size and volume fraction of the strengthening precipitates. The heterogeneous mode of deformation would enable stress or strain concentration at the particle interface and aid in void nucleation; alternately, brittle cracking could occur due to stress enhancement in the vicinity of the particle. For the homogenous mode of deformation, such as occurs in overaged or Mn containing alloys, stress and strain fields are expected to be less intense or more relaxed due to the dispersion of slip. This could lower void nucleation and growth rates and delay void link-up. The areal void density results, suggest that for alloy #1, the number and nucleation rate of voids is lower, and their growth more stable in the overaged than in the underaged condition. This results in a higher fracture strain for the overaged alloy.

Normally, the link-up or coalescence of voids occurs by intense strain localization of the material between voids. The intensity or concentration of slip is controlled by the strengthening precipitates and the nature of the dispersoids. In aluminum alloys the overaged condition leads to nonshearable precipitates, and the presence of Mn dispersoids also result in homogenization of slip. In the underaged condition increasing the Mn level would increase homogenization of slip and, therefore,

should delay the link-up process. In the overaged condition the critical void volume fractions are observed to be higher than in the underaged condition due to the nonshearable precipitates and further homogenization of slip by Mn containing particles.

5. CONCLUSIONS

Ductile fracture in 2134 type aluminum alloys has been studied in under- and overaged conditions for alloys containing 0%, 0.31%, 0.61% and 1.02% Mn. The ductility of smooth specimens in the overaged condition was observed to be higher than for the underaged condition; however, notched specimens exhibit lower ductility in the overaged condition consistent with fracture toughness results.

In the smooth specimens, the critical void volume fraction, i.e., the volume fraction of voids beneath the fracture surface, was always higher in the overaged case. The void volume fraction results, together with areal void density and rate of void growth results, suggest that the curtailment in ductility in the underaged alloys is due to easier link-up of voids, through localized slip between voids. The enhancement in ductility in the overaged condition is due to a delay in link-up of the voids.

The effect of Mn additions is to increase the void volume fraction, areal density of voids and also void growth rates; however, the critical parameters, i.e., critical void volume fraction, critical number density of voids and critical void size, are highest for the highest Mn content and not always necessarily lowest for the lowest Mn alloy. Thus the effect of Mn is rather complex. The ability of Mn to increase the degree of

homogeneous deformation and raise the volume fraction of void nucleating particles produces competing effects which dictate the link-up process.

It is clear from the present investigations that triaxiality does not increase the void nucleation rate. The void growth rate and link-up process are substantially accelerated at the high triaxiality level resulting in low fracture strain.

6. References

1. R.H. VanStone, R.H. Merchant and J.R. Low: "Fatigue and Fracture Toughness-Cryogenic Behaviour," ASTM STP 556, 1974, p. 93.
2. R.H. VanStone, T.B. Cox, J.R. Low and J.A. Psioda: International Metals Review 30, No. 4, 1985, p. 157.
3. A.S. Argon, J. Im, and A. Needleman: Metall. Trans. A 6 , 1975, p. 815.
4. A.S. Argon, J. Im and R. Safoglu: ibid., p. 825.
5. A.S. Argon and J. Im: ibid., p. 839.
6. J.W. Hancock and M.J. Cowling: Metal Science, 1980, p. 293.
7. J.W. Hancock and A.C. Mackenzie: J. Mech. Phys. Solids 2, 1976, p. 147.
8. J. Rice and D.M. Tracey: J. Mech. Phy. Solids 17, 1969, p. 201.
9. G. Leroy, J.D. Embury, G. Edwards and M.F. Ashby: Acta. Metall. 29, 1981, p. 1509.
10. A. Gysler, G. Lutjering and V. Gerold: Acta. Metall. 22, 1974, p. 901.
11. E.P. Butler, N.J. Owen and D.J. Field: Mater. Sci. & Tech. 1, 1985, p. 531.
12. M.F. Ashby: Phil. Mag. 14, 1966, p. 1157.
13. P.W. Bridgeman: Trans. ASM, 32, 1944, p. 553.
14. R.O. Ritchie, W.L. Server and R.A. Wullaert: Metall. Trans. A 10, 1979, p. 1557.

TABLE 1
Actual Chemical Composition of the
Alloys Studied in Weight Percent

Alloy	Si	Fe	Cu	Mn	Mg	Ti	Zr	Al
#1	0.04	0.06	3.96	---	1.48	0.01	0.14	bal.
#2	0.04	0.06	3.96	0.31	1.46	0.01	0.12	bal.
#3	0.04	0.06	4.18	0.60	1.46	0.01	0.11	bal.
#4	0.04	0.06	4.51	1.02	1.47	0.02	0.12	bal.

TABLE 2
Grain Sizes (ASTM E112)

Alloy	/	1	2	3	4
D _{eq} (μm)	/	185	275	248	211
G _{eq}	/	1.53	0.37	0.66	1.13

TABLE 3
Large Particle Distribution and Spacing Parameters

Alloy	V_V	$N_A (\text{mm}^{-2})$	$N_T (\text{mm}^{-1})$	λ (mm)	σ (mm)
#1	0.0175	589	5.2	0.19	0.19
#2	0.0196	686	5.5	0.18	0.18
#3	0.0220	722	6.63	0.15	0.15
#4	0.0407	1129	10.6	0.091	0.095

TABLE 4
Starting Triaxialities

	R_O (in)	a_O/R_O^*	σ_T/Y
T_O	∞	0	0.333
T_1	1.5	0.057	0.361
T_2	0.437	0.197	0.427
T_3	0.174	0.5	0.556
T_4	0.044	2.0	1.02
T_5	0.0095	9.2	2.06

TABLE 5
Room Temperature Mechanical Properties

Alloy	σ_{ys} (MPa)	σ_{uts} (MPa)	n	%E	ϵ_f	%RA	K_Q (MPa \sqrt{m})
#1 UA	376	431	0.052	11.2	0.409	33.7	52
OA	447	481	0.036	13.5	0.573	43.2	39
#2 UA	403	443	0.065	15.7	0.444	37.4	53
OA	448	478	0.037	10.3	0.644	48.8	45
#3 UA	414	498	0.060	9.8	0.377	37.7	52
OA	467	512	0.053	11.7	0.421	42.1	44
#4 UA	425	491	0.057	13.4	0.217	17.8	32
OA	451	493	0.041	9.5	0.305	26.2	27

TABLE 6
Nucleation Curve Fit ($y=mx$)

Alloy	m	s
1UA	662	30
2UA	578	58
3UA	763	112
4UA	3314	52
10A	246	30
20A	430	144
30A	768	137
40A	3579*	147

m = slope or $\frac{\text{voids/mm}^2}{\text{unit strain}}$
S = standard deviation

*40A curve fit for $y=mx+b$, where $b=-234$.

TABLE 7
Void Growth Rates*

Alloy	VGR($\epsilon = 0.1$)	VGR($\epsilon = 0.2$)	VGR($\epsilon = 0.3$)	VGR($\epsilon = 0.4$)
1UA	11	14	23	64
2UA	7	9	15	54
3UA	7	9	17	50
4UA	21	272	--	--
10A	8	11	13	17
20A	7	7	12	19
30A	12	19	28	
40A	15	36	208	--

*VGR = $dL_{\max}/d\epsilon$

TABLE 8
Triaxility and Corresponding Fracture Strain

Condition	R_0	$(a/R)_0$	(σ_T/Y)	ϵ_f
T ₀ -UA	∞	0	0.333	0.377
T ₀ -OA	∞	0	0.333	0.421
T ₂ -UA	11	0.2	0.427	0.298
T ₂ -OA	11	0.2	0.427	0.294
T ₃ -UA	4.4	0.5	0.556	0.308
T ₃ -OA	4.4	0.5	0.556	---
T ₄ -UA	1.1	2.0	1.02	0.230
T ₄ -OA	1.1	2.0	1.02	0.161
T ₅ -UA	0.24	9.0	2.04	0.115
T ₅ -OA	0.24	9.0	2.04	0.053

TABLE 9
Nucleation Curve Fit for Triaxial Samples
($y=mx$), Alloy #3

Sample	m	S
TO-UA	763	112
T4-UA	676	22
T0-OA	768	137
T4-OA	915	19

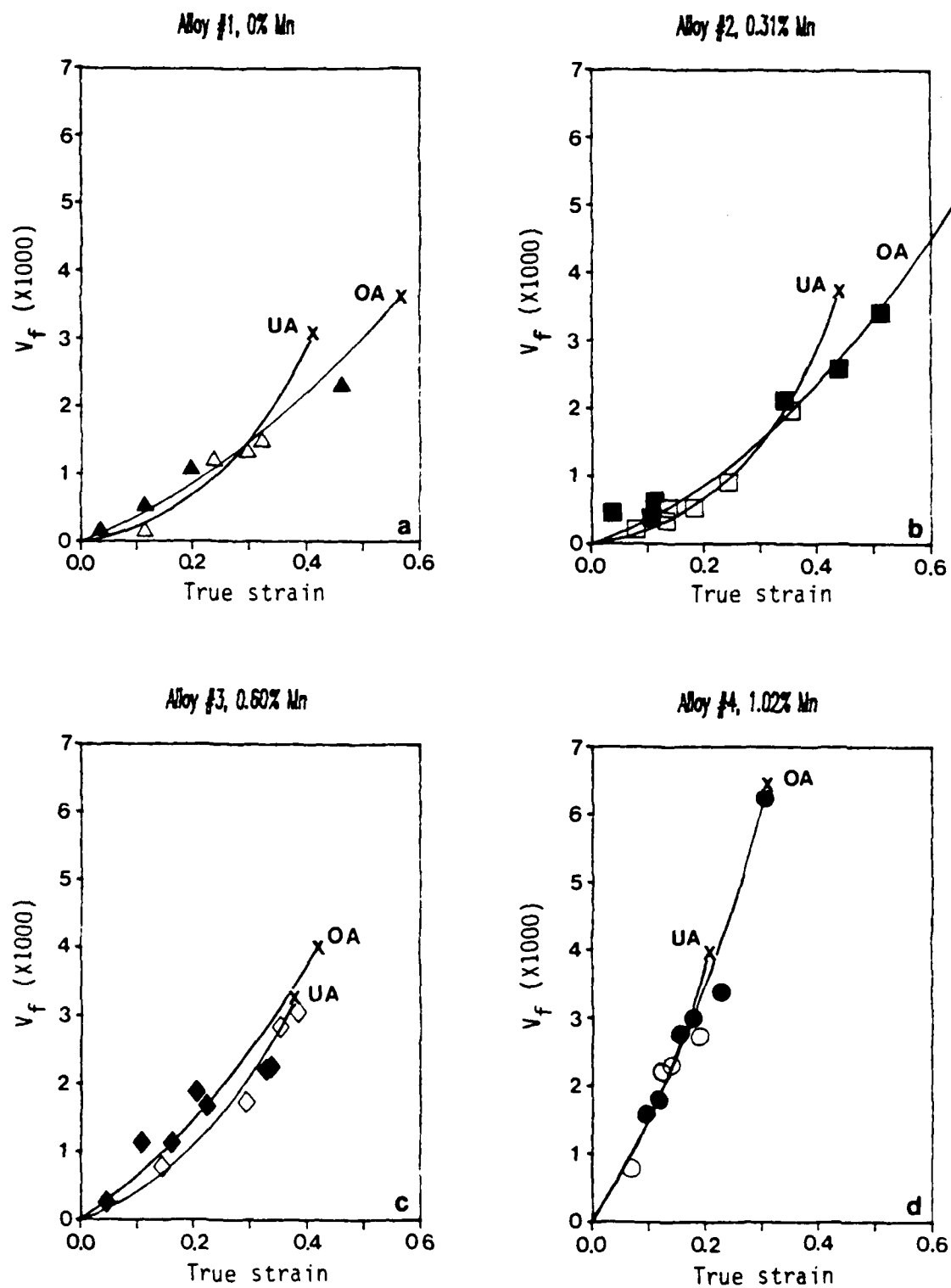


Figure 1 . Void volume fraction vs. true strain,
(a) #1, (b) #2, (c) #3, (d) #4

Void volume fraction vs. strain

Pycnometer data, UA

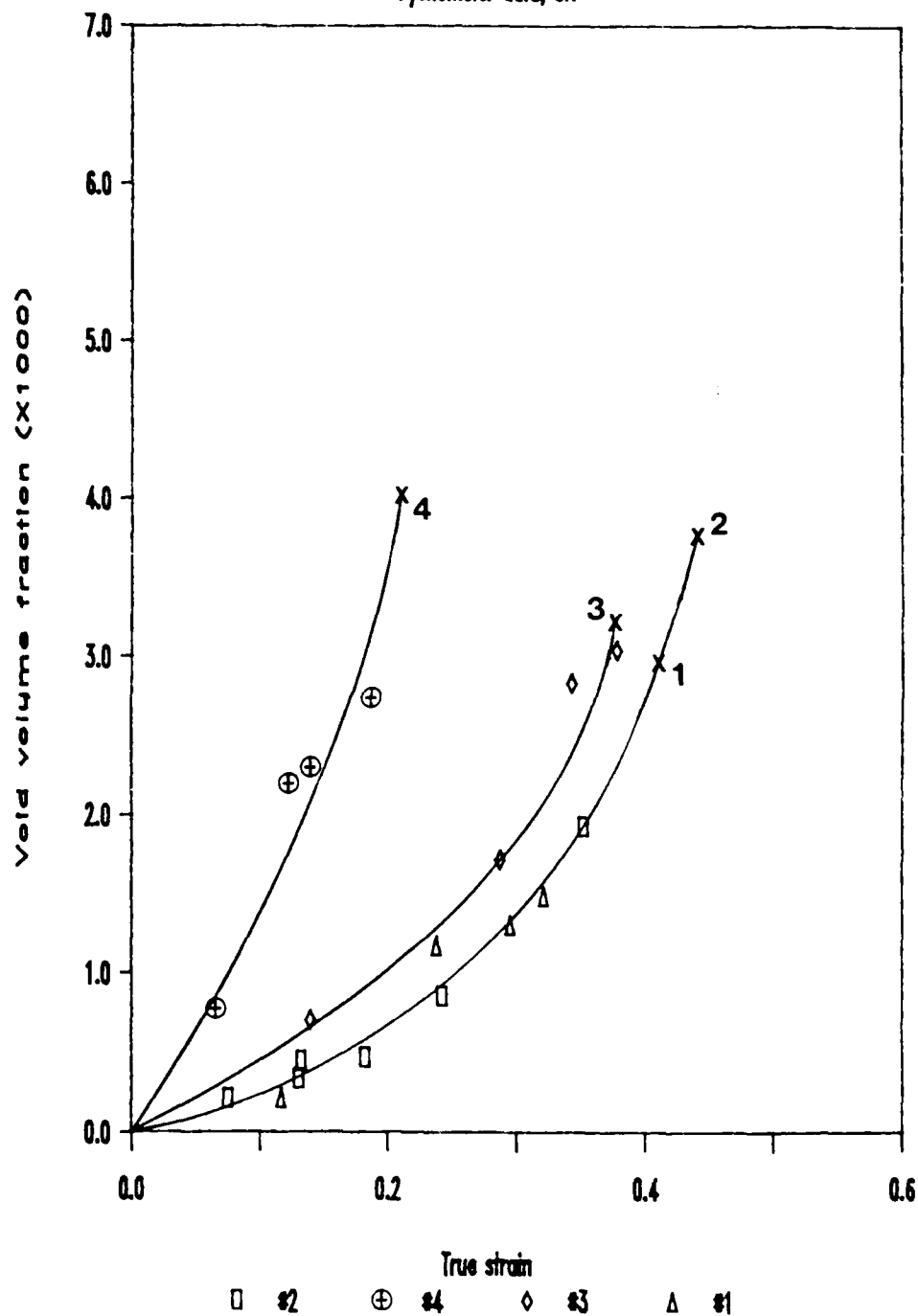


Figure 2. Void volume fraction vs. true strain: UA

Void volume fraction vs. strain

Pycnometer data, OA

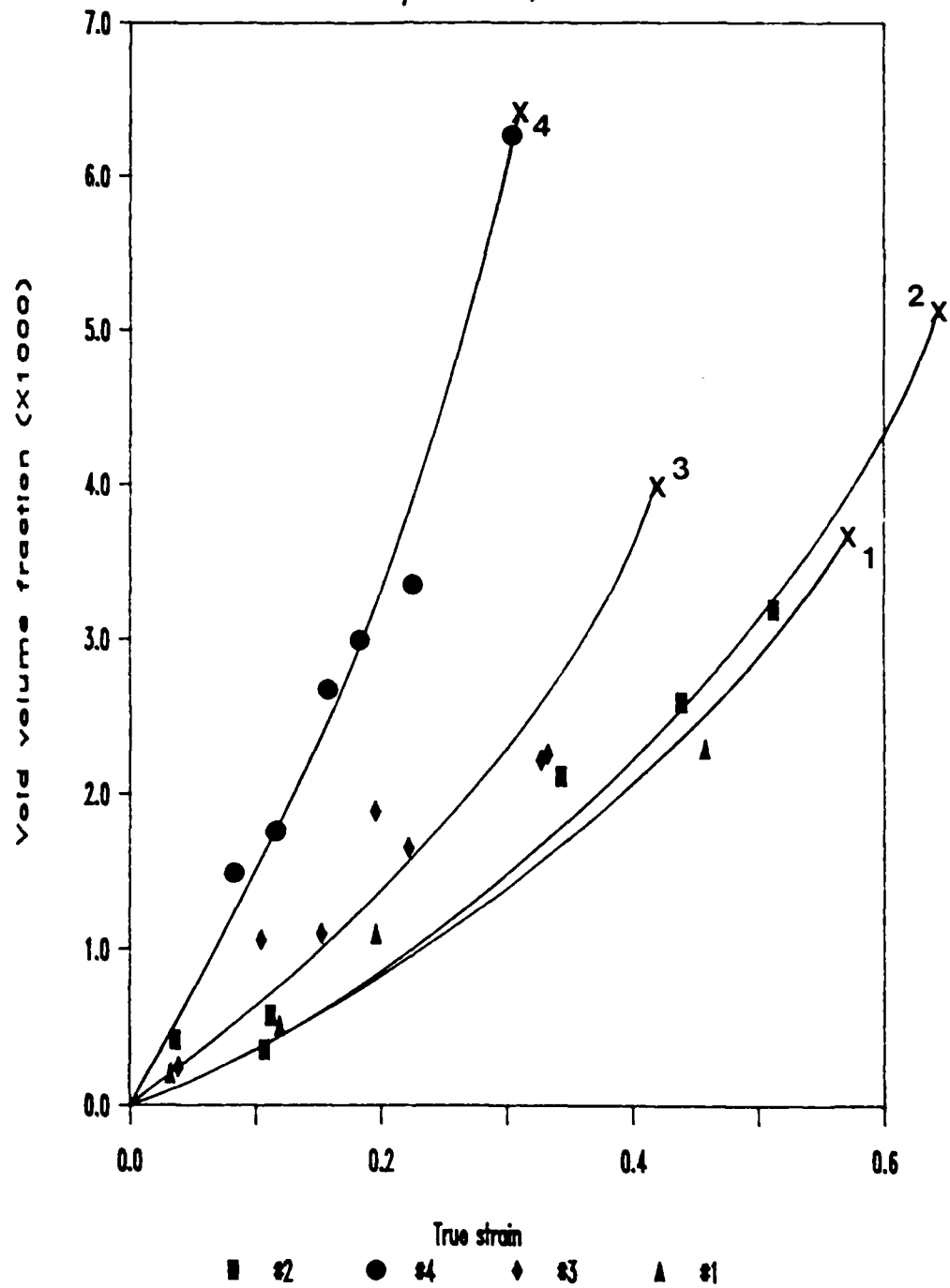


Figure 3. Void volume fraction vs. true strain: OA

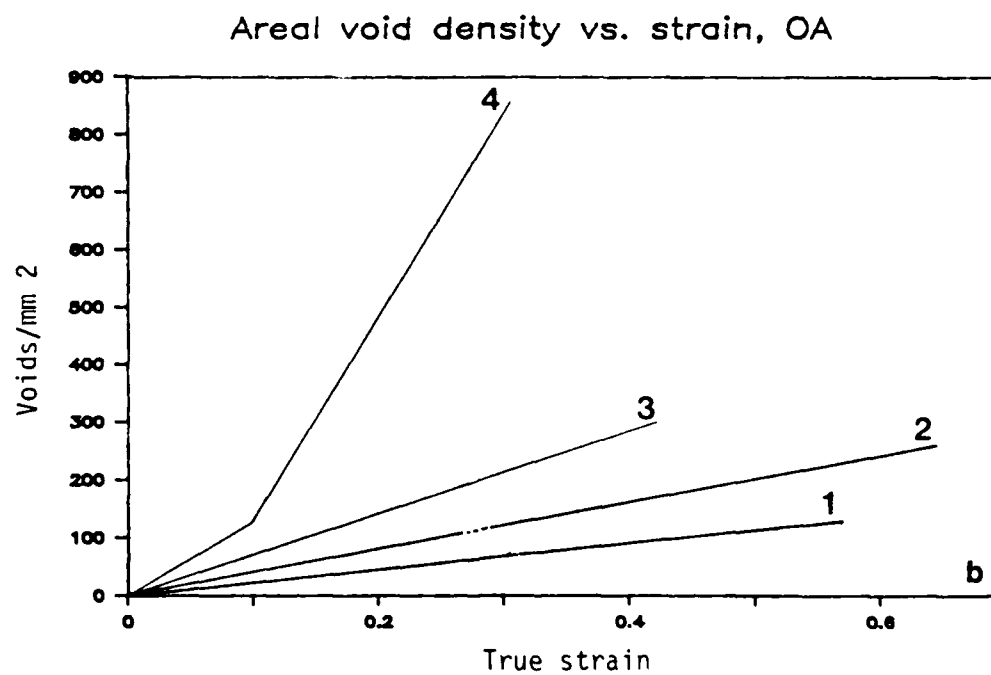
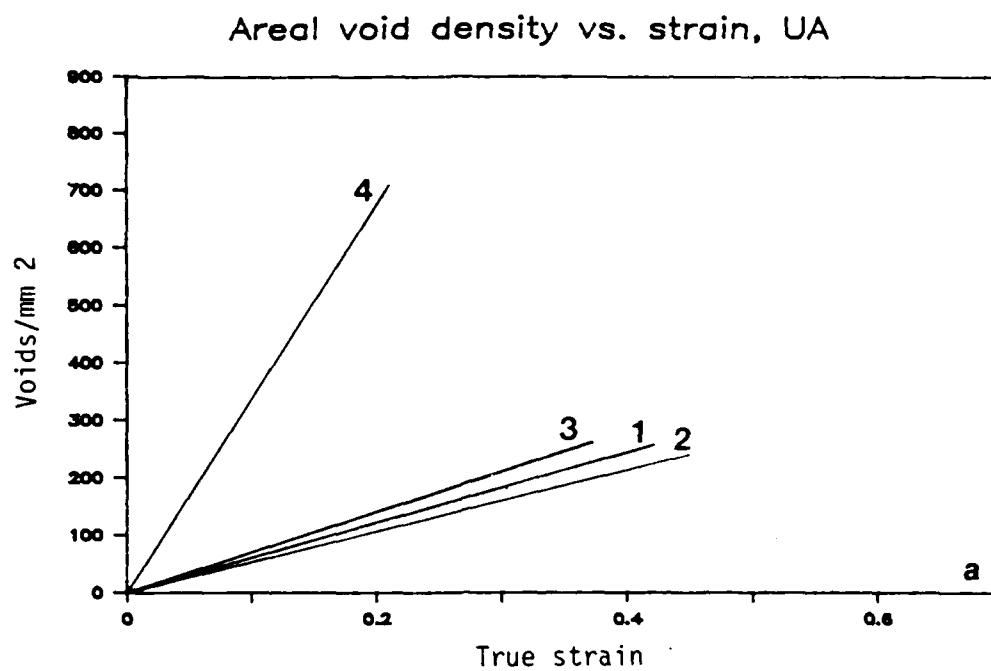


Figure 4. Areal void density vs. true strain showing increasing nucleation with deformation, (a) UA, (b) OA

Lmax vs. strain

Underaged alloys

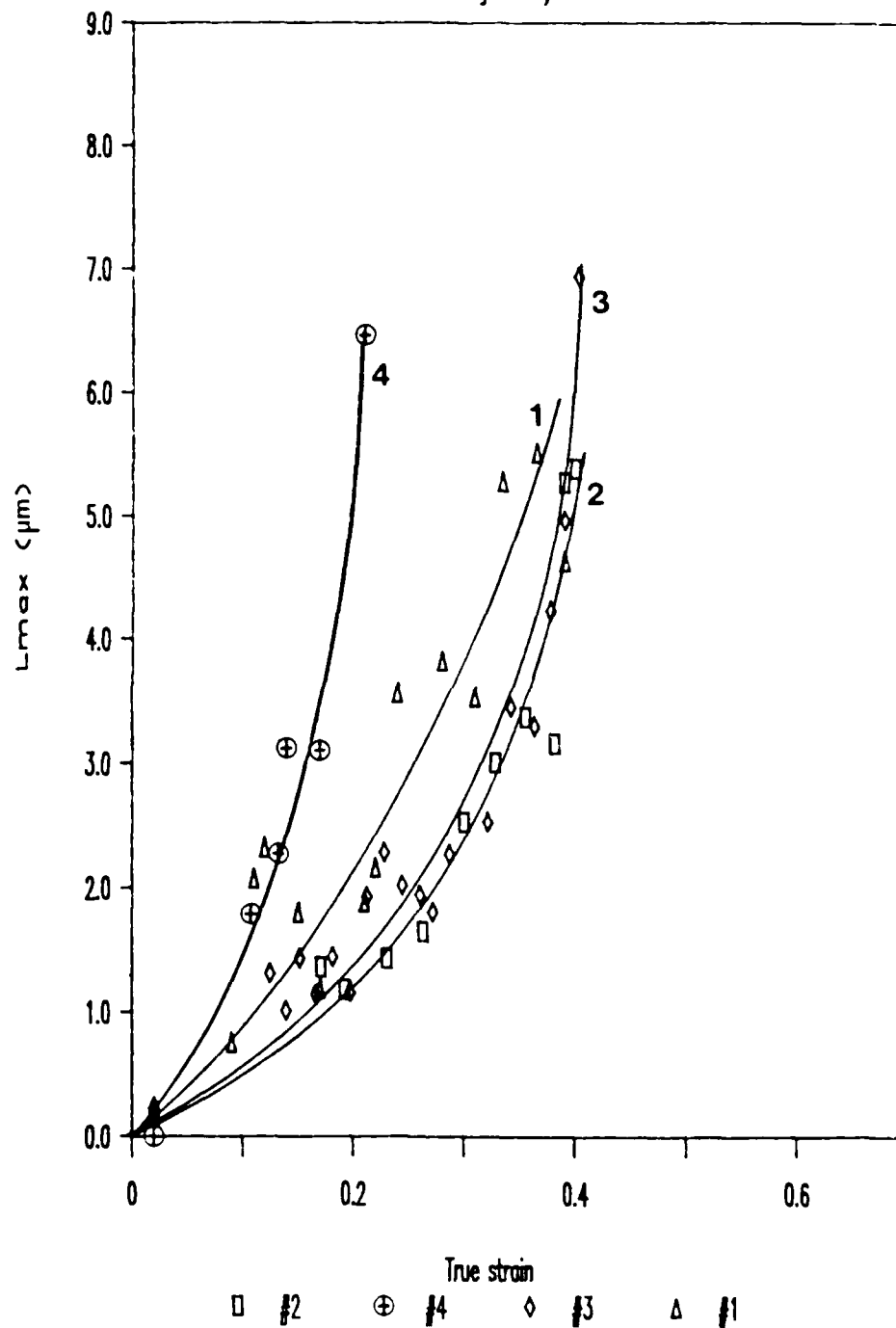


Figure 5. L_{max} vs. true strain : UA

L_{max} vs. strain

Overaged alloys

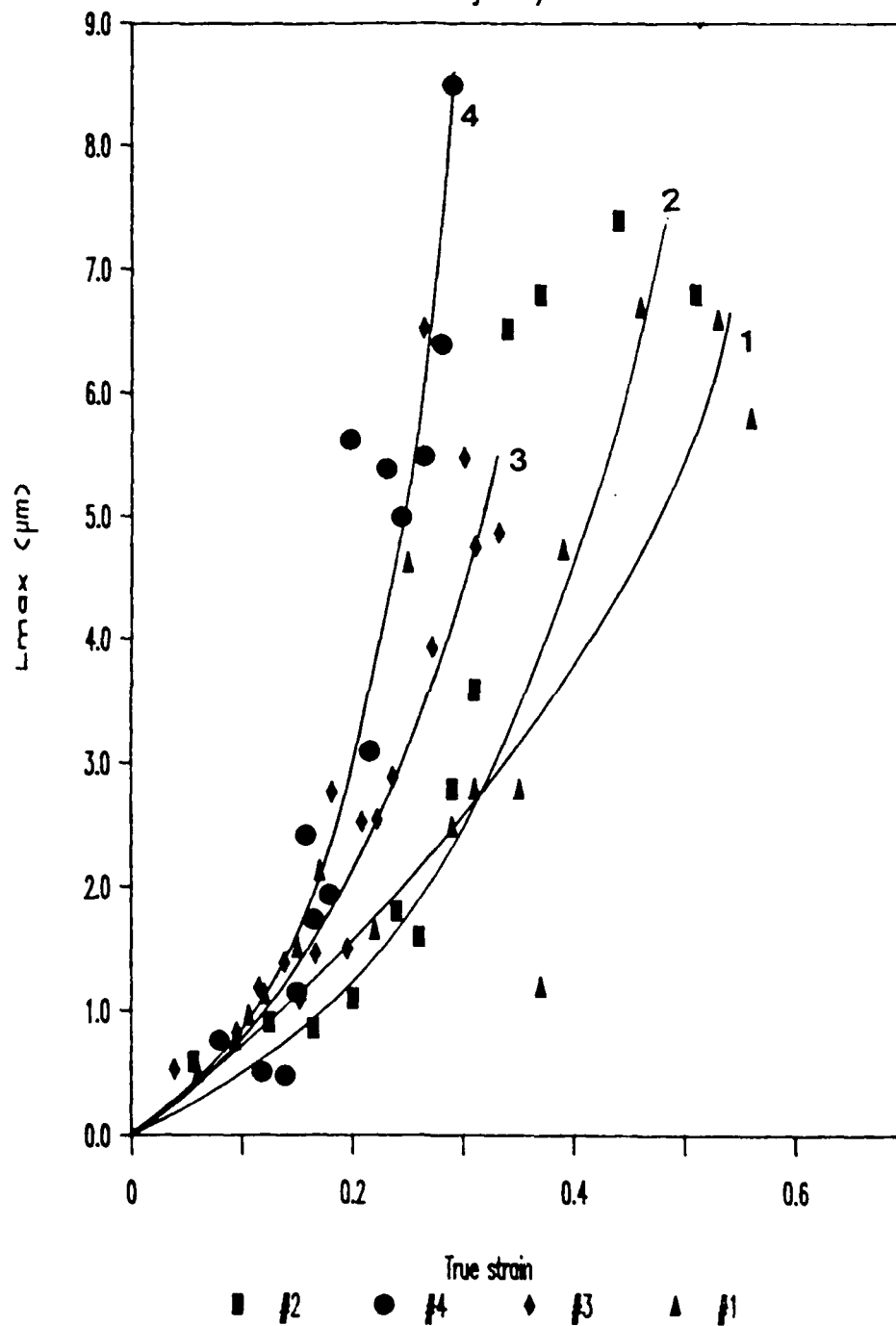


Figure 6. L_{max} vs. true strain : OA

Fracture strain vs. triaxiality

#3 alloy (0.60% Mn)

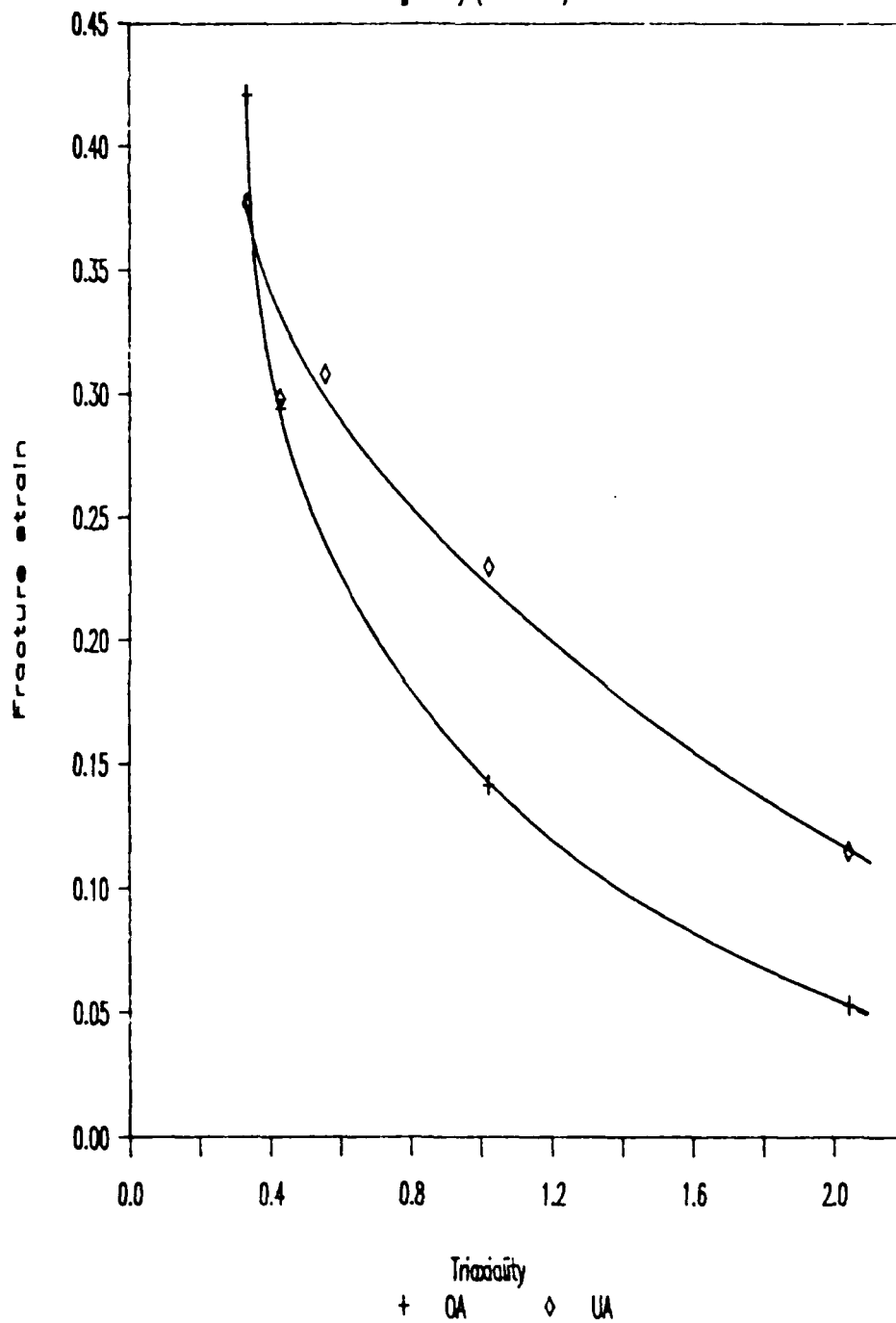


Figure 7. Fracture strain vs. triaxiality for #3 alloy

Void volume fraction vs. strain

#3 underaged

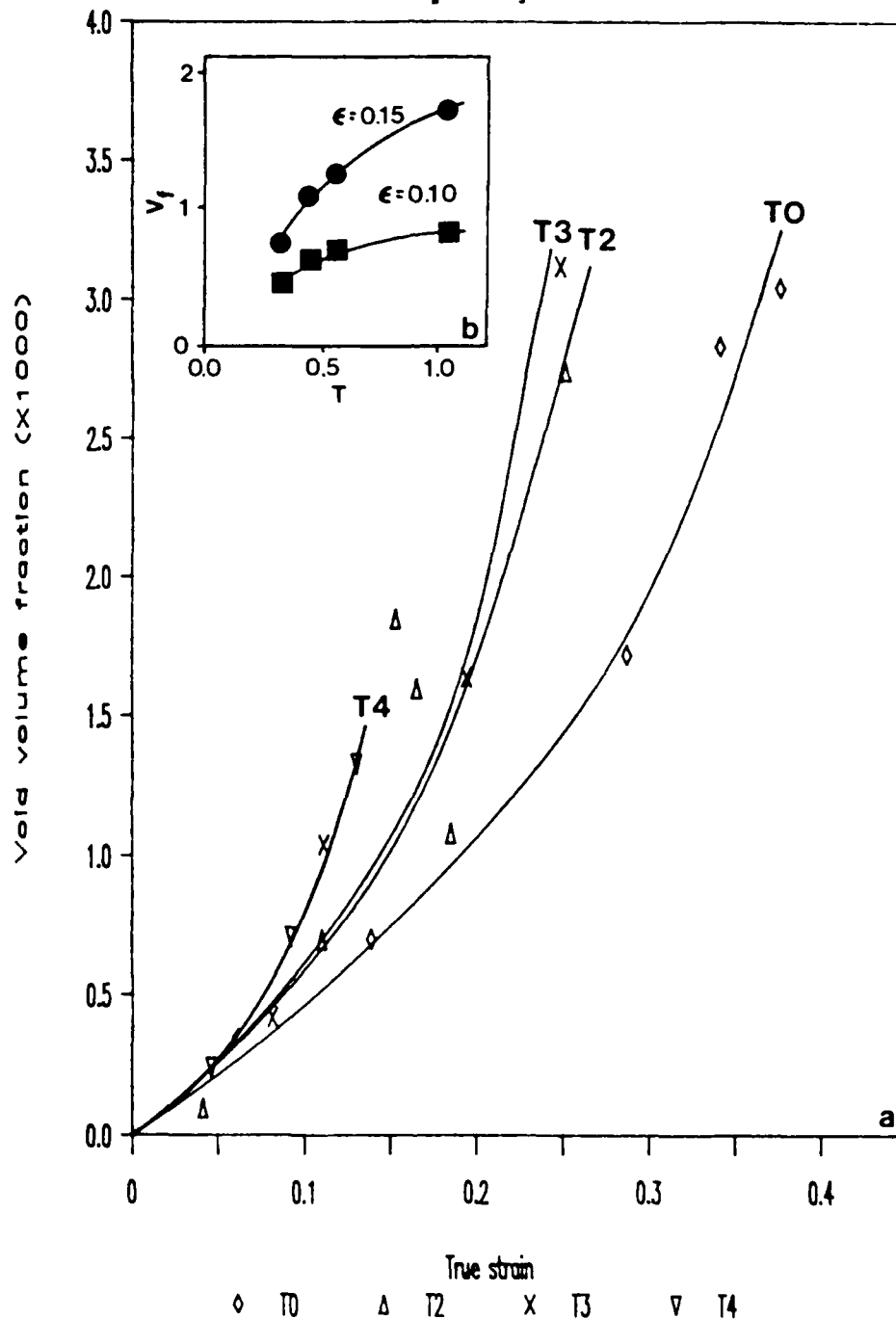


Figure 8 (a) Void volume fraction vs. true strain for notched specimens: 3UA, (b) V_f vs. triaxiality at $\epsilon = 0.10$ and 0.15

Void volume fraction vs. strain

#3 overaged

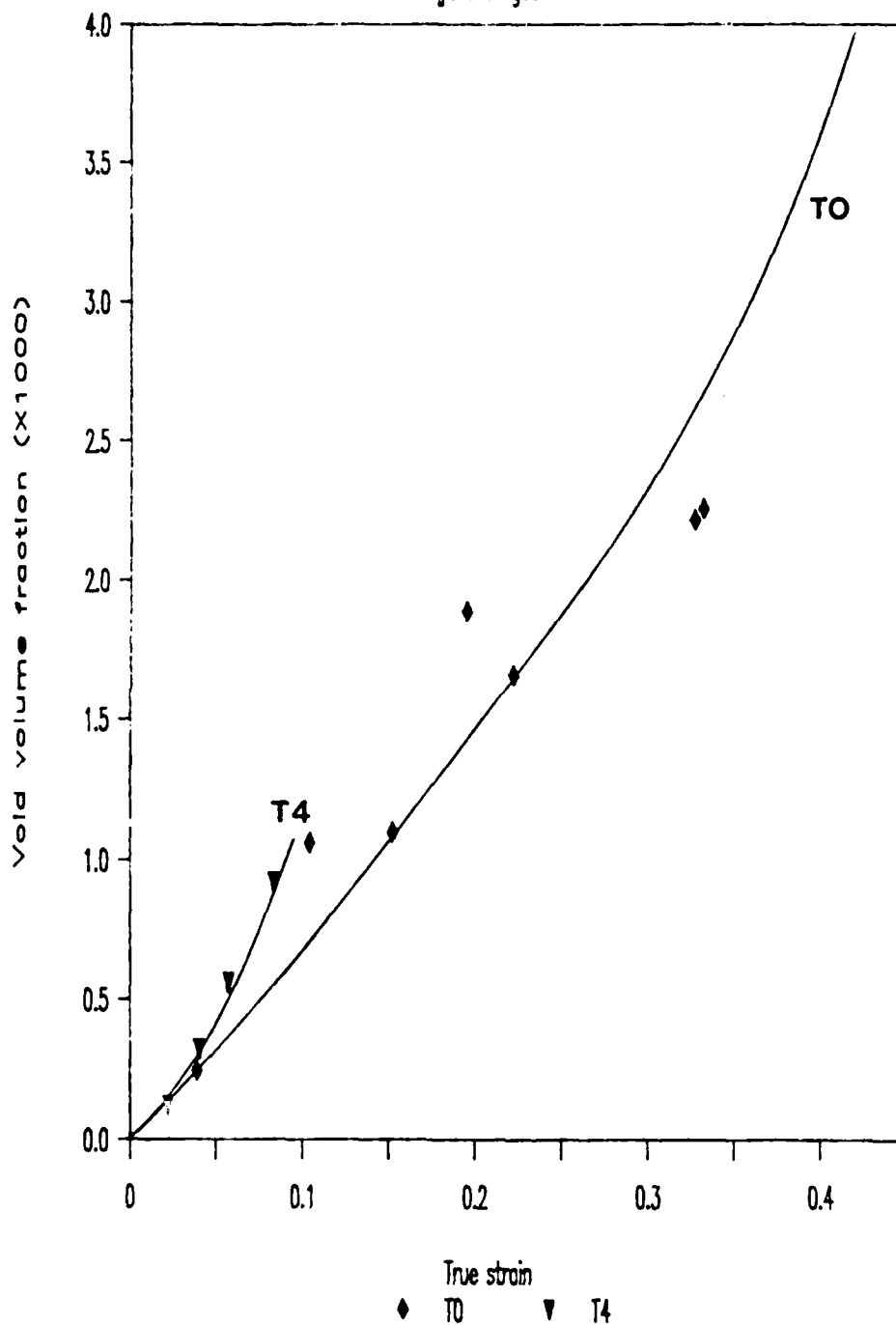


Figure 9 Void volume fraction vs. true strain for notched specimens : 30A

Void volume fraction vs. strain

#3-T4

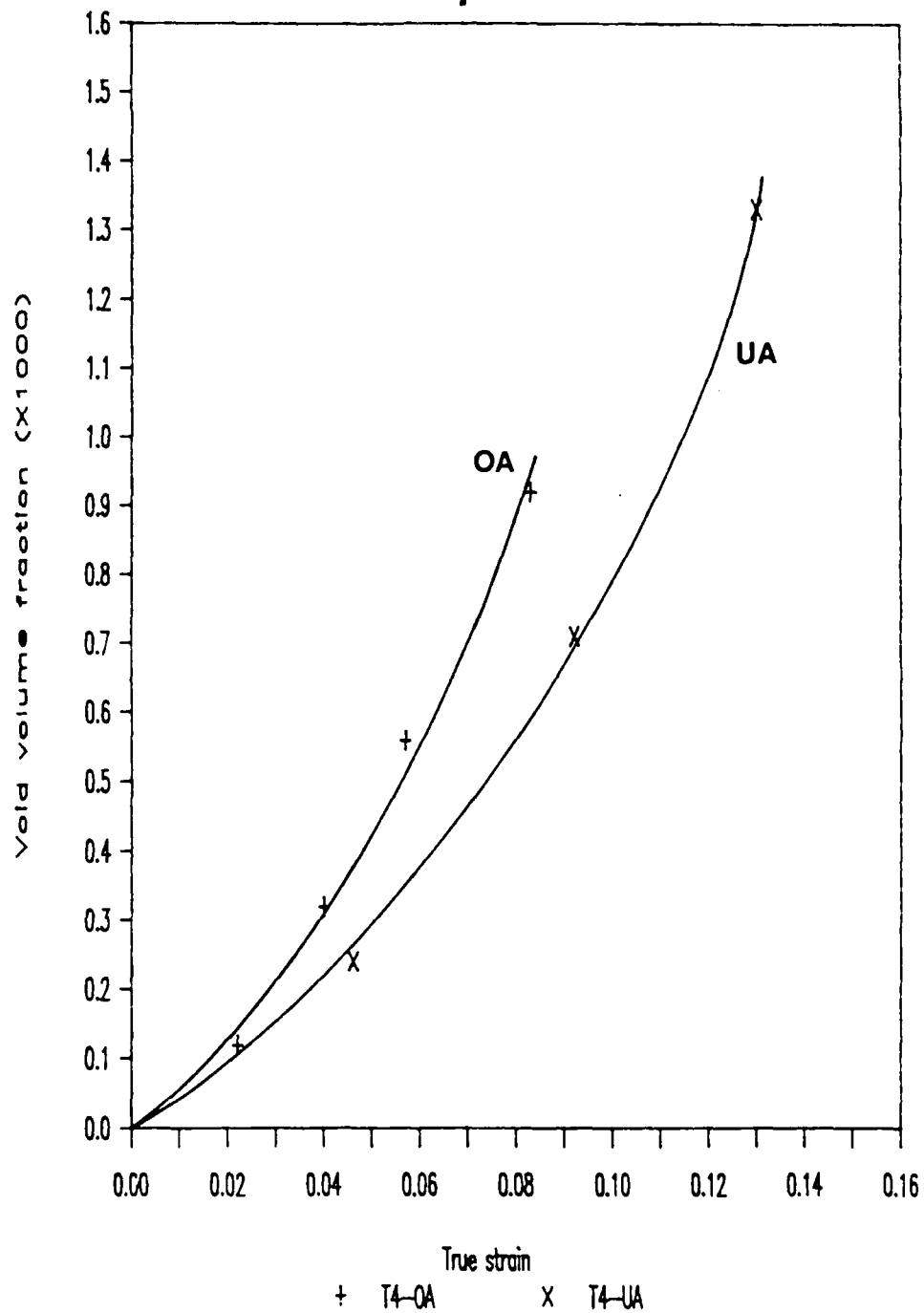
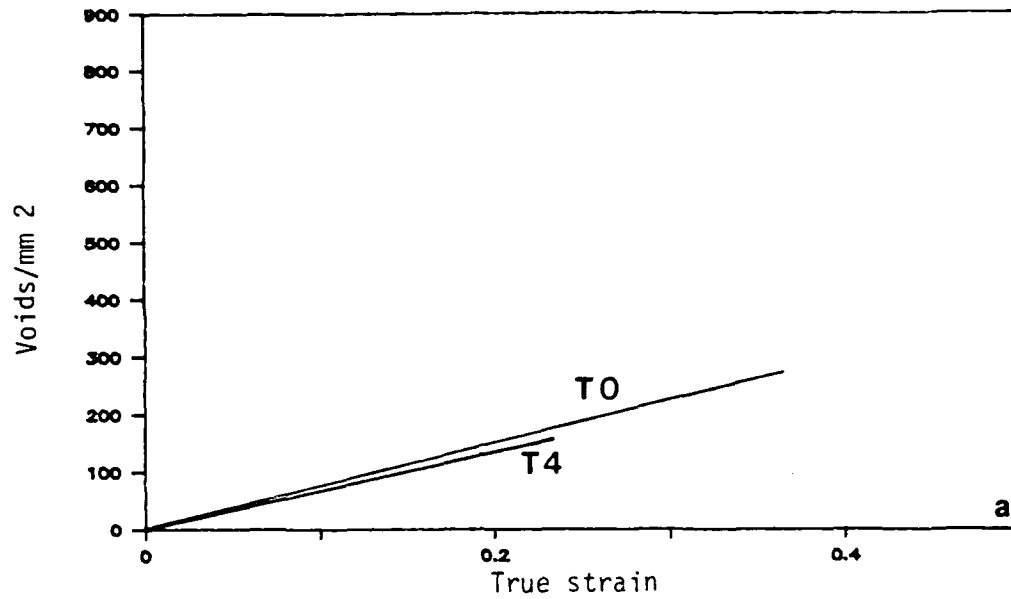


Figure 10 . Void volume fraction vs. true strain : T4

Areal void density vs. strain, 3LUA



Areal void density vs. strain, 3LOA

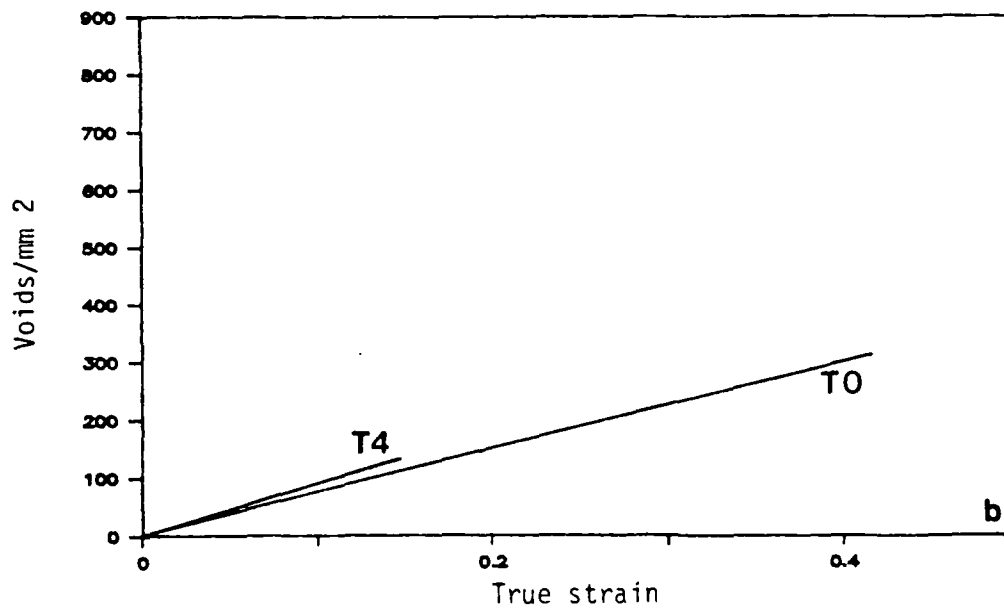


Figure 11. Voids/mm² vs. strain for notched specimens : #3

Max. void length vs. strain

3LUA-T0,T4

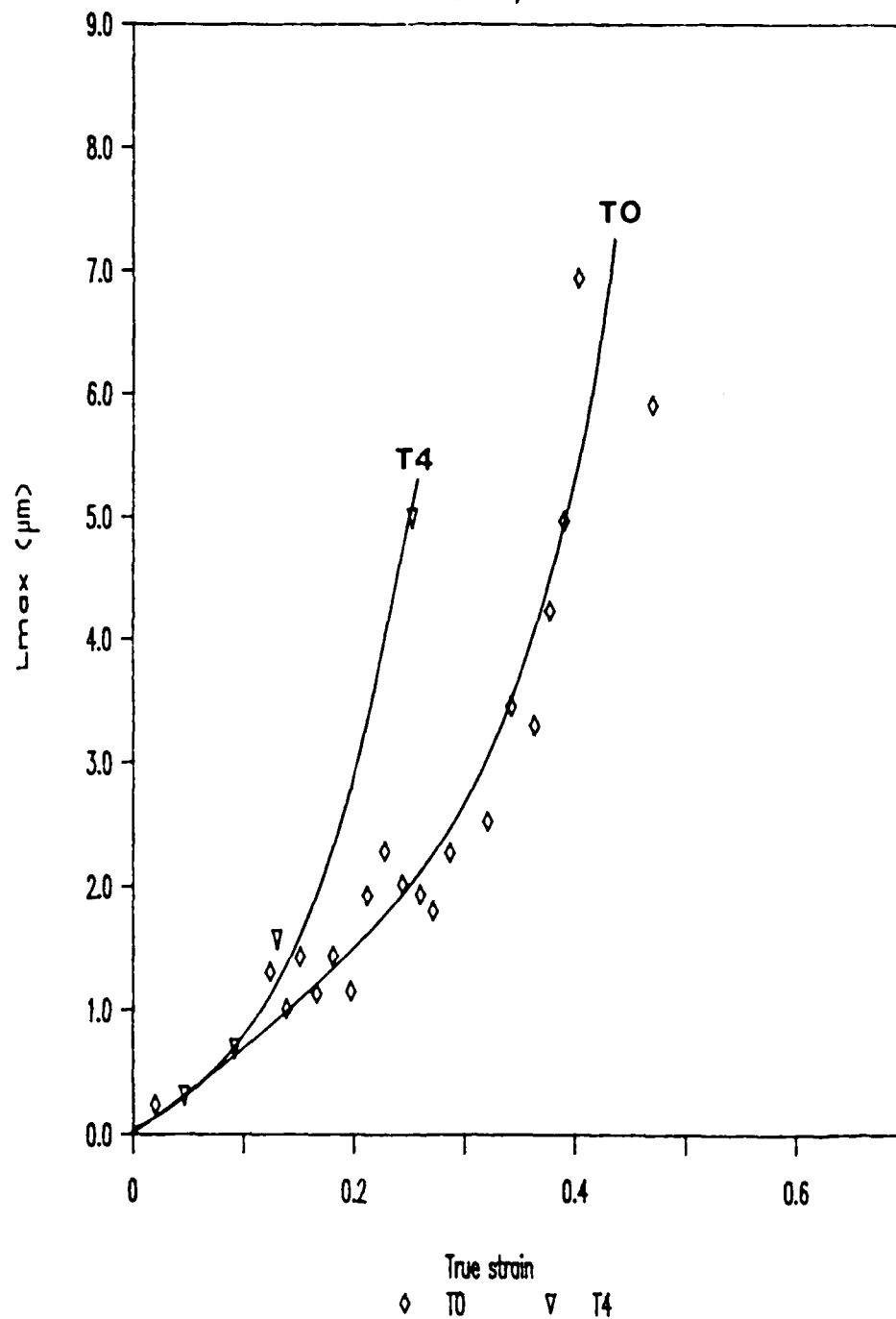


Figure 12. L_{max} vs. strain for notched specimens: 3LUA

Max. void length vs. strain

30A-T0,T4

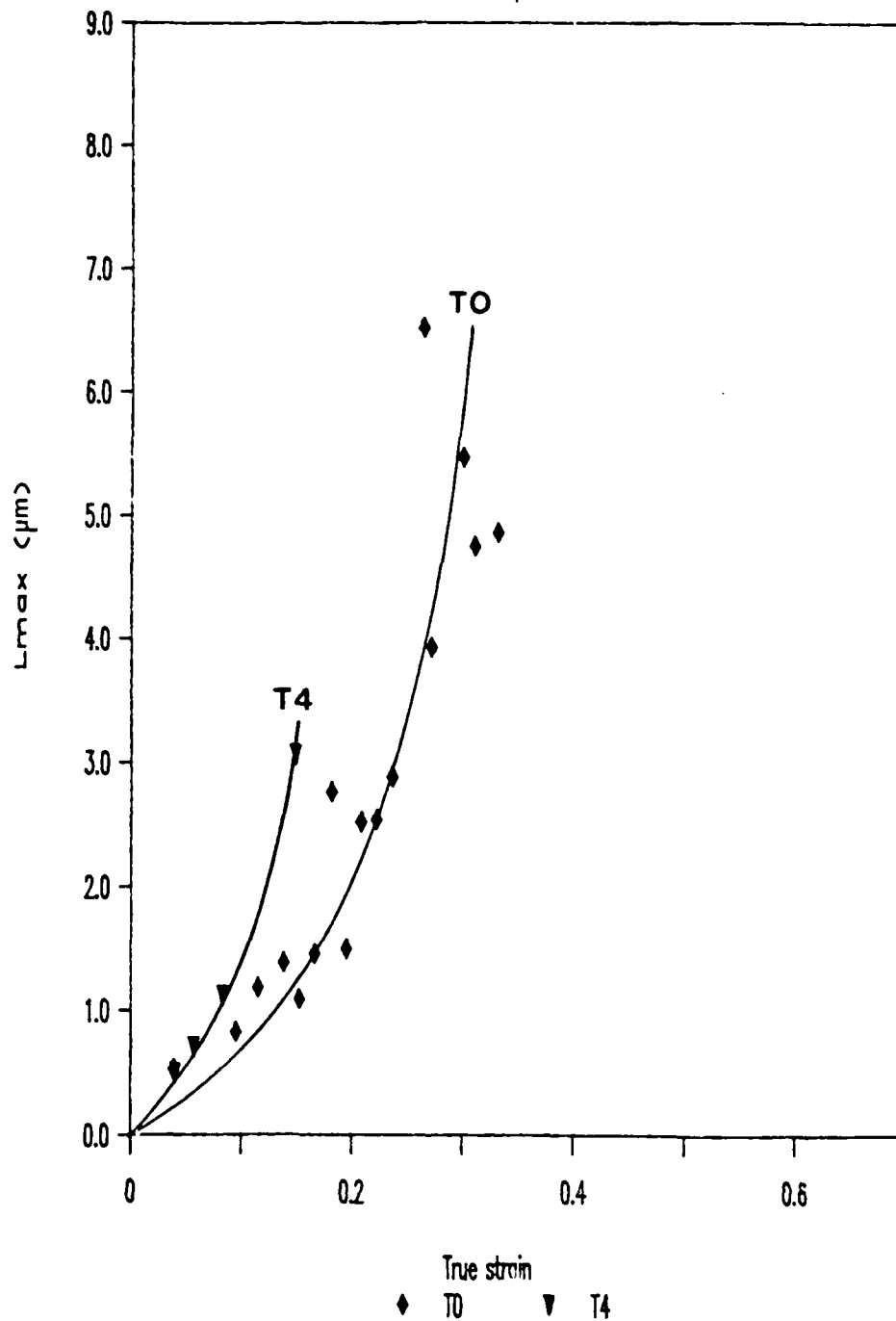


Figure 13. L_{max} vs. strain for notched specimens: 30A

PART II. PROCESSING OF ADVANCED ALUMINUM ALLOYS FOR STRUCTURE CONTROL

H. Gudmundsson and J.A. Wert

The goals of Part II of this investigation are to identify the recovery and recrystallization mechanisms that operate during processing of new aluminum alloys as they relate to material and processing parameters. During the current reporting period, this study has focused on Al-Si-Zr and Al-O-C alloys that contain a high density of dispersoids. These are model materials that exhibit the desired range of microstructural relaxation mechanisms, but avoid complications such as precipitation that are present in technologically-important alloys with similar dispersoid contents. Studies on Al-Si-Zr and Al-O-C alloys have shown that the microstructural evolution during annealing is strongly dependent on the homogeneity of the dispersoid distribution and on the degree of cold deformation. Processing conditions have been found that lead to predominately continuous rather than discontinuous evolution on the cold worked microstructure during annealing. We are currently conducting quantitative analysis of the microstructure to establish the extent of continuous recrystallization as a function of dispersoid content; initial results are reported here. We have also found that concurrent annealing and deforming gives rise to a more rapid continuous recrystallization process. It is believed that continuous recrystallization during concurrent annealing and deformation is responsible for observations of superplasticity at high strain rates; we expect to identify and model these processes during the course of this research.

1. Introduction

The goals of Part II of this investigation are to identify the recovery and recrystallization mechanisms that operate during processing of new aluminum alloys, to understand how material and process parameters influence these mechanisms, and ultimately to develop a model capable of predicting grain size and grain boundary characteristics from the important material and processing variables.

The research objectives can be reformulated as fundamental questions about the evolution of aluminum alloys during processing:

i. What mechanisms contribute to evolution of a subgrain structure into a grain structure during annealing of aluminum alloys containing high levels of dispersoid particles?

ii. Which material and processing parameters control this evolution?

Once these questions have been answered, a model for processing will be developed to permit prediction of the combinations of material parameters and processing conditions that will produce desired grain morphologies.

Many alloys produced by rapid solidification or other PM methods (including atomization, planar flow casting and mechanical alloying) contain high volume fractions of small particles. Once formed, these particles cannot be dissolved and reprecipitated, although they often coarsen to some extent during annealing (such as during hot vacuum degassing of powder compacts). When consolidated by hot deformation, a sufficiently high dislocation density is introduced to provoke

recrystallization under normal circumstances. However, when the density of dispersoid particles is high, nucleation of recrystallized grains is suppressed and conventional recrystallization does not occur. Instead, a more gradual process of subgrain boundary migration and subgrain coalescence occurs, eventually leading to a microstructure which contains moderately high-angle grain boundaries. This process has been termed continuous recrystallization or in situ recrystallization [1-5], even though it falls outside of the ordinary definition of recrystallization as defect elimination through migration of high-angle boundaries.

Examples of aluminum alloys which are thought to exhibit continuous recrystallization are shown in Table I. This table shows that many types of aluminum alloys currently under development derive their room temperature strength in large part from the fine grain or subgrain size produced by recovery and/or recrystallization processes. Superplastic properties of all of these alloys depends almost exclusively on the grain structure developed during processing. Consequently, a model capable of predicting the effects of processing parameters on the evolution of a subgrain structure toward a continuously-recrystallized grain structure in aluminum alloys containing high volume fractions of dispersoid particles would be of considerable value. The goals of this research program are to identify the mechanisms of continuous recrystallization in high dispersoid-content aluminum alloys; to establish the material and processing parameters that control continuous recrystallization; and to

synthesize a model to predict the effect of key material and processing parameters on grain size, grain boundary characteristics and mechanical properties.

TABLE I
Examples of Aluminum Alloys that Exhibit
Continuous Recrystallization

Alloy	Composition	Strengthening Mechanism(s)
Supral	Al-Cu-Zr	Precipitation
--	Al-Fe-Ce	Dispersoid + subgrain
IN-9052	Al-Mg-O-C	Dispersoid + subgrain
IN-9021	Al-Cu-O-C	Dispersoid + subgrain
--	Al-Li-X-Zr	Precipitation

2. Technical Background

Grain size and grain boundary characteristics strongly influence material properties, affecting how metals are fabricated and how they perform in a service environment [6,7]. In aluminum alloys of current or near-term technological importance, the grain structure is produced by one of the two recrystallization processes. The only practical way to control recrystallization in aluminum alloys is through the use of particles [8,9]. This background section outlines our current understanding of the influence of particles on recrystallization processes, and describes how processing methods for grain size control can be designed to take advantage of these effects.

2.1 Particle Effects on Recrystallization

Numerous studies have established that recrystallizing grains nucleate in deformation zones that form around hard particles during deformation [10-15]. However, to create a

deformation zone with sufficient lattice rotation to produce a viable nucleus, a particle must exceed a minimum diameter (d_c). Particle dispersions also create drag pressure on migrating boundaries [16-19]. Particle-induced drag pressure restricts boundary motion during both recrystallization and subsequent grain growth.

Sections 2.2 and 2.3 describe how these particle effects on recrystallization are used to control grain size by both of the recrystallization processes described previously.

2.2 Grain Size Control by Discontinuous Recrystallization

TMPs that employ discontinuous recrystallization for grain size control in precipitation-hardening aluminum alloys operate by introducing a high density of particles larger than the critical diameter, thereby providing a high density of nucleation sites for recrystallizing grains. Since d_c is near 1 μm for heavily-rolled polycrystalline aluminum [11-15], most constituent particles are larger than d_c and thus serve as nucleation sites for recrystallizing grains. However, the density of constituent particles is usually insufficient to yield recrystallized grain sizes smaller than about 25 μm [20-22].

To provide additional sites for nucleation of recrystallizing grains, TMPs that operate by discontinuous recrystallization include treatments which precipitate the soluble alloying elements as particles larger than d_c . Since the density of such precipitate particles is ordinarily much higher than that of constituent particles, precipitate particles provide a large increase in the density of potential nucleation sites for

recrystallizing grains.

The dispersoid particles present in most precipitation-hardening aluminum alloys are much smaller than d_c and therefore do not create sufficiently intense deformation zones to stimulate nucleation of recrystallized grains. However, dispersoid particles create a significant boundary drag pressure, unlike the coarser particles which are too large to make a substantial contribution to boundary drag pressure unless their volume fraction is substantial.

TMPs that operate by discontinuous recrystallization were originally developed by experimentation, but they may now be understood and analyzed by considering the effects of particles on recrystallization and on grain growth. Synthesis of such a TMP for AA7475 and evaluation of the property changes produced by this process have been the subject of a prior AFOSR contract [23]. In commercial alloys that contain several types of particles, the effects of alloy composition and TMP parameters on grain size are not always evident from fundamental principles. Consequently, models capable of predicting recrystallized grain size as a function of various alloying and TMP parameters are useful tools for TMP design and optimization.

Nes [24-26] and Sandstrom [27] proposed models for calculating recrystallized grain size in alloys containing particles either larger than, or smaller than, d_c . Later work by Nes extended these models to include alloys containing particles larger than d_c along with smaller particles which create boundary drag pressure [28-30]. Recent publications by Nes, Wert and coworkers [9,31,32] have described models which include all

classes of particles present in commercial heat-treatable aluminum alloys. These latter models are sufficiently sophisticated to aid design and optimization of TMPs for commercial alloys.

2.3 Continuous Recrystallization

Continuous recrystallization is an alternate recrystallization path which does not proceed by nucleation and growth of new grains. Instead, continuous recrystallization occurs by a gradual process of subgrain growth or coalescence, leading to formation of high-angle grain boundaries without requiring high angle boundary migration [1-5]. The mechanism which allows subgrain growth or coalescence to produce high angle boundaries has not been well established, although the process is thought to involve subgrain boundary migration. As subgrain boundaries migrate, the subgrain size increases and the average boundary misorientation increases. Eventually, when moderate or high misorientations have developed, subgrain growth ceases. The subgrain boundary migration process appears to be assisted by simultaneous deformation at the annealing temperature. During annealing without simultaneous straining, changes in misorientation and subgrain size occur considerably more slowly.

To obtain continuous recrystallization, the much more rapid discontinuous recrystallization process must be suppressed. This requires boundary drag pressures sufficient to prevent nucleation of discontinuous recrystallization. Particle dispersions with P_z in excess of 800 kPa can provide the necessary drag forces, suggesting that continuous recrystallization should only be

observed in alloys containing very high densities of small particles. Indeed, the most well known examples of continuous recrystallization in aluminum are alloys containing high densities of Al_3Zr dispersoids [18,33-35] or PM alloys containing high densities of several types of fine particles.

With such high boundary drag pressures needed to suppress discontinuous recrystallization, it seems surprising that sufficient migration of low-angle boundaries to produce continuous recrystallization can occur. Thus, other mechanisms which could allow low-angle boundary migration in the presence of high drag pressures have been proposed. Alborn, Hornbogen and Koster [1] suggested that subgrain boundary migration can occur when particle coarsening leaves some subgrain boundaries weakly restrained. Alternatively, straining during annealing may provide added driving pressure for boundary migration, accelerating continuous recrystallization. Work by Nes cited previously demonstrates the effect that elevated temperature straining can have on the kinetics of continuous recrystallization. However, these suggestions are largely speculative at the present time.

2.4 Regimes of Continuous and Discontinuous Recrystallization

As previously described, dispersoid particles influence both continuous and discontinuous recrystallization through the drag pressure they impose on boundaries. Indeed, dispersoid drag pressure is the key material parameter that controls which of the two recrystallization paths will be followed. The effect can be viewed as shown in Fig. 1, where recrystallized grain size (d_R)

and average boundary misorientation after annealing (θ_R) are sketched as a function of drag pressure. The process type is defined at the top of these diagrams. Dotted lines indicate uncertainty or absence of experimental data.

At low drag pressures, discontinuous recrystallization operates because the drag pressure is sufficiently low to permit nucleation of recrystallizing grains. Dependence of grain size on drag pressure is fairly certain in this regime [9,32]. Both modeling and experimental results indicate that the trends are correct, although data are limited at higher drag pressures within the discontinuous regime.

At very high drag pressures, recovery is allowed but recrystallization does not occur. Drag pressure is so large that reorganization of the dislocation cell structure into a subgrain structure is slow. Once formed, the subgrain boundaries are essentially immobile. This result is experimentally confirmed by experimental observations on mechanically-alloyed materials containing very high volume fractions of carbide and oxide particles which provide the high drag pressures characteristic of this regime.

At intermediate drag pressures, in the continuous recrystallization regime, our understanding of the effect of drag pressure on grain size and boundary misorientation is limited. The effects illustrated in Fig. 1 are largely speculative, and the roles of other material and processing parameters in this regime are virtually unknown. The reason for this uncertainty is twofold. First, alloys with dispersoid drag pressures within the

continuous recrystallization regime have only recently emerged as commercially-important alloys. Second, the mechanisms do not fit neatly into the classical categories of discontinuous recrystallization and recovery. Continuous recrystallization probably occurs by a mix of mechanisms borrowed from the classical recrystallization and recovery processes. It is identification of the basic mechanisms and their integration into a predictive processing model that are the focus of Part II of the current contract.

3. Progress During the Current Reporting Period

3.1 Alloy Preparation

Alloys with three compositions providing a variation of boundary drag pressure have been selected for study and have been obtained from various sources. (The two Al-Zr-Si alloys were kindly provided by Reynolds Metals Company and the mechanically-alloys Al-O-C alloy was contributed by Inco Alloys International). The chemical compositions of these alloys are listed in Table II. The first two alloys below have been prepared and are currently being studied. Of the two Al-Zr alloys the one with higher Zr content has shown a tendency toward discontinuous recrystallization at lower annealing temperatures and it will not be studied further.

TABLE II
Alloys Compositions and Characteristics

Alloy	Drag pressure	Method of preparation
Al-0.90-1.2C	1.4 MPa*	Mechanical alloying
Al-0.26Zr-0.1Si	0.58 MPa*	DC casting
Al-0.45Zr-0.1Si	1 MPa	--

*Measured

**Estimated

3.2 Microstructure of Al-Zr and Al-O-C alloys

Since the dispersoid particles play a key role in the evolution of structure during processing, it is essential to characterize the particle distributions in the materials under study. This section describes the results of those analyses.

3.2.1 Heat treatment of Al-Zr alloys for formation of dispersoid particles.

Al-0.26Zr-0.1Si: No Al_3Zr primary particles (diameter normally > 1 micrometer) could be seen in the specimens (dimensions 11x15.5x55.6 mm) chosen for heat treatment. The as-cast grain size was coarse (grain diameter near 1-2 mm) and stayed constant during the heat treatment. To precipitate the small coherent Al_3Zr particles, specimens were heated to 450°C at a rate of 50°C/hr and held at 450°C for 8 hours [36]. After this treatment, small coherent Al_3Zr precipitates were observed in the specimens by TEM (Fig. 2). The mean particle radius after heat treatment is 5 nm and the distribution of the particles has been observed to be dependent on the local solidification rate.

By etching a heat treated cross section (1:10 NaOH/H₂O, 70°C) from the edge of a direct chill casting a dendritic

structure appeared (Fig. 3). Qualitative Energy Dispersive X-ray analysis done with an SEM showed that the light areas in the figure contain more Zr and Si than the darker areas. In this alloy the Zr tends to segregate to areas that solidify first (dendrites), while the Si should segregate to areas that solidify last. The Si atoms are thought to aid precipitation of the Al_3Zr particles [36] and they might also affect the segregation of the Zr during solidification. Earlier investigators have suggested that Cu affects segregation of Zr in an Al-6Cu-0.5Zr alloy [33].

The size and spacing of the Zr enriched dendrites have a strong effect on the deformation and annealing behavior of the alloy, as discussed later.

Al-0.45Zr-0.1Si: Sections chosen from the most rapidly solidified parts of the ingot showed coarse primary Al_3Zr particles (Fig. 4). No TEM studies have been done on this alloy since it exhibited discontinuous recrystallization behavior at relatively low annealing temperatures. The coarse primary particles are thought to be the cause of this since they act as nucleation sites for discontinuous recrystallization and also deplete the matrix of Zr thereby lowering the drag pressure from dispersoids.

3.2.2 Dispersoid distribution in Al-O-C alloy.

Figure 5 shows the dispersoids and grain structure after an 8 hour anneal at 600°C . Annealing eliminates excess dislocations which makes the study of the dispersoid distribution easier. The effect, if any, of the anneal on the grain structure is uncertain since the as-extruded microstructure has not been studied yet.

The mean linear intercept size of the grain structure is around 0.5 micrometers.

The Al_2O_3 and Al_4C_3 dispersoids can have different shapes and sizes in mechanically alloyed aluminum [37,38]. The majority of oxide particles are equiaxed with irregular edges (Type A in Fig. 5), while flake-shaped oxide particles (type B) are also present. Previous investigators [38] have reported that the smallest particles (radius < 15 nm) in mechanically-alloyed aluminum are a mixture of oxides and carbides while the carbides have been reported to have a mean radius of 3.5 nm. The oxides in this material are sometimes observed in clusters which then have to be regarded as single large particles.

Values of the drag pressure from the dispersoid particles in the Al-O-C alloy have been determined as shown in Table III. In the calculations, it was assumed that all spherical particles with radius < 10 nm are carbides. These assumptions probably lead to an underestimate of the drag pressure from the dispersoids. Adding up the contributions from the two kinds of dispersoids to the drag pressure gives a value of about 1.4 MPa which is certainly a minimum value. By using a value of 4 nm for the carbide mean radius [37] the value increases to 2.6 MPa.

TABLE III
Drag pressure (P_z) parameters in Al-0.90-1.2C

	Volume fraction (f)	Mean radius (r) [nm]	(f/r) [m^{-1}]	P_z [MPa]
Al_2O_3	0.013	24	$5.5 \cdot 10^5$	0.12
Al_4C_3	0.044	8	$5.5 \cdot 10^6$	1.25

3.3 Deformation and annealing of Al-Zr and Al-O-C alloys.

After establishing the types of dispersoid particles in the alloys under investigation, the deformation and annealing microstructures have been studied. Results from these experiments are reported in section 3.3

3.3.1 Cold rolling and subsequent annealing of Al-Zr alloys.

Heat treated specimens of Al-Zr-Si were cold rolled in 10% increments of reduction. After each rolling pass the specimen was cooled with water to reduce recovery during rolling and the specimens were stored in a freezer after rolling. Sections from the rolled specimens were annealed in air for 8 hours at temperatures up to 450°C. Three categories of material have been studied:

- A) 11x15.5x55.5 mm piece from the chill zone of a direct chill cast ingot, Al-0.24%Zr-0.1%Si (*)
- B) 11x15x55.5 mm piece from a thin chill cast ingot, Al-0.26%Zr-0.1%Si (**)
- C) 11x15.5x55.5 mm piece from the chill zone of a direct chill cast ingot, Al-0.45%Zr-0.1%Si (**)

(*) Composition from chemical analysis.

(**) Nominal composition.

Sample A solidified more rapidly than sample B, leading to a more uniform distribution of Zr and Si in the as-cast microstructure even though the average composition is the same. Sample C exhibited discontinuous recrystallization at relatively low temperatures and the as-rolled hardness was similar to that for B. As mentioned previously, studies of sample C have not

been continued.

Figure 6 shows the hardness as a function of annealing temperature for an 8 hour anneal in air. Increased solidification rate and rolling reduction raises the hardness value for the as-rolled material. The hardness measurements were done on longitudinal cross-sections in all cases. The indentations were made at the half thickness location on a section normal to the rolling direction. For sections from B this is where the segregation of Zr is the greatest (i.e. maximum spacing between Zr rich dendrites) while sections from A show very little difference in segregation between surface and center. This segregation effect accounts for the observed difference in the softening behavior of A and B materials.

3.3.2 Microstructure after cold rolling.

Figure 7 shows how Zr rich dendrites act as hard "islands" in the matrix and how deformation bands flow around them. With increasing rolling reductions the dendrites become more flat and the spacing between them decreases. Figures 8a and 8b show better how deformation cells flow around the Zr rich dendrites and how the high density of Al_3Zr dispersoids delays the formation of deformation cells. The deformation cells around the dendrites also contain dispersoids but the density is not as high.

3.3.3 Microstructure evolution during annealing.

The microstructural evolution during annealing is very dependent on segregation and the degree of deformation with material A showing the most gradual change and the most homogeneous microstructure.

Figure 9a shows nucleation of discontinuously recrystallized grains around dendrites after an 8 hour anneal at 350°C in a 75% rolled material (B). That seems to indicate that the hard dendritic areas are initiating discontinuous recrystallization and that the particle density between the dendrites is not sufficiently high to retard the migration of high angle boundaries. Figure 9b shows the microstructure in a 90% rolled material (B) after the same heat treatment. Very few large grains had nucleated and TEM observations revealed a substructure in various stages of recovery.

Annealing 90% rolled material of type A and B at 400°C leads to an approximately 65% drop in hardness. However, A shows however less nucleation of large grains (Figure 10). TEM observations of material A after that heat treatment revealed a well-polygonized microstructure where medium angle boundaries (10-30° misorientation) are common. Figures 15 and 16 show the microstructure and misorientations found with convergent beam analysis. Of 22 boundaries analyzed, 10 have misorientations between 10 and 30°. The figures show that in some places a moving boundary has dissolved the Al₃Zr particles. Behind these boundaries various needle-shaped and larger particles can be seen. This phenomena has been observed before and it is suggested that it is more favorable for the coherent Al₃Zr particles to dissolve rather than being forced into an incoherent state by the passing of a boundary [39]. The particles can then discontinuously precipitate behind the moving boundary [40] and retard its movement if the retarding force is high enough.

Figure 11 shows some places where a boundary has freed itself from precipitates and migrated further.

Annealing 90% rolled material A at 450°C leads to an almost fully recrystallized structure with an average grain size of 50 micrometers (as determined by optical microscopy). At higher temperatures the microstructure has less chance to recover and reduce the driving force for recrystallization. Where the particle density is low, a grain can at high temperatures rapidly gain a size and misorientation advantage and start migrating into the substructure.

TEM observation of annealed materials demonstrate that segregation of Zr leads to formation of hard regions in the microstructure that subsequently act as nucleation sites in the Al-0.26Zr-0.1Si. Between these hard regions, the dispersoid particle density is lower. Thus, a discontinuously recrystallized grain can nucleate in deformation zones surrounding the hard regions and can quickly grow into the surrounding dispersoid-depleted region. This type of discontinuous recrystallization process is reasonably well-understood and we seek to avoid this situation in our studies of continuous recrystallization.

By reducing the segregation of Zr and rolling to 90% reduction the distribution of Al_3Zr particles becomes more more uniform, thereby reducing the width of areas of low particle density. This reduces the size (at least in the short transverse direction) that a nucleated grain can quickly grow into. Thus, our studies of continuous recrystallization will focus on the Al-Zr-Si alloy with the highest cooling rate during solidification,

and with 90% reduction during cold rolling.

A few specimens of this material have been analyzed after annealing. These observations show that roughly half of the boundaries in this material have misorientations exceeding 10° , while the other half have lower misorientations. Further analyses of these heat treatment conditions are underway, and we shall determine the kinetics of evolution of the subgrain boundary structure present after cold rolling into the partially continuously recrystallized structure that we have observed after long annealing times.

3.4 Concurrent annealing and deformation of Al-Zr-Si.

Continuous recrystallization proceeds at a faster rate if the sample is simultaneously strained and annealed than if it is annealed without straining. We have begun a series of observations which are designed to identify the mechanism producing this effect.

Material of type A was cold rolled to 90% reduction and machined to make tensile specimens for high temperature deformation. The tensile specimens have a 35 mm gauge length with a 12.9 x 8 mm cross section. A thermocouple was attached to the sample with a wire and it placed in specially made grips on an Instron machine equipped with a three zone furnace. Two tests have been made with a strain rate of $6.5 \times 10^{-4} \text{ sec}^{-1}$ at 400°C . In both cases the sample was in a cold rolled state before the test and reached the testing temperature in one hour. After being stabilized at 400°C for 20 minutes, it was strained to about 60% elongation before the test was stopped, the sample removed from

the grips and quenched in water.

Figure 12 shows both the engineering stress-strain curve and the true stress - true strain curve for the second test. As can be seen, the true stress decreased after about 6% strain and continued decreasing. A negative slope of the true stress - true strain curve shows that the material is recovering or recrystallizing during deformation.

Figure 13 shows the microstructure in both the gauge and grip sections of the tensile sample. While the undeformed sections appears to have a recovered or partially recrystallized microstructure, the deformed section shows a markedly different structure. Elongated grains (100-200 micrometers long) appear to be surrounded by small (10 micrometer diameter) grains. TEM studies are being conducted to characterize these features on a finer scale.

The results obtained so far suggest that straining during annealing markedly increases the rate of continuous recrystallization. Further tests are planned to establish the degree to which the continuous recrystallization kinetics are accelerated, and to find whether the concurrent deformation produces effects that are not observed at all in samples that are annealed without concurrent deformation.

3.5 Deformation and annealing of Al-O-C alloy.

Table IV summarizes the annealing and deformation experiments done on the Al-1.2C-0.90 alloy up to now.

TABLE IV
Hardness values for various heat treatments
and deformations for Al-1.2C-0.90 (5kg/30sec)

Treatment	Hardness [MN/m ²]	% Softening
As extruded	960.3 +/- 7.6	-
1 hr 630°C	789.3 +/- 17	18 +/- 2
8 hrs 600°C	832.9 +/- 16	13 +/- 2
18 hrs 530°C	899.1 +/- 6.7	6 +/- 3
18 hrs 530°C + 30% cold rolling	897.4 +/- 13.7	7 +/- 2
18 hrs 530°C + 60% rolling	855.1 +/- 15.4	10 +/- 2

Annealing at 630°C leads to the formation of almost 1 mm long cracks oriented in the longitudinal direction. The cracks are also present after annealing at 600°C, although they are considerably smaller than at the higher annealing temperature (about 20 micrometers long). The cracks are due to the expansion of H₂ and H₂O gas trapped in the oxide layer of the aluminum powder used for mechanical alloying. Poor degassing of the aluminum powder is the cause of this problem. Annealing at 530°C did not lead to visible cracking.

An experiment has been performed to reproduce an observation reported with the mechanically-alloyed alloy IN 9051 [41]. That alloy showed a marked increase in hardness after rolling and then showed catastrophic grain growth after a 1 hr anneal at 375°C. However, the Al-1.2C-0.90 alloy did not show work hardening for cold rolling to 60% reduction so there is no increase in the driving force for recrystallization. Since the grain/subgrain

size is very small (0.5 micrometers), it is likely that slip length is on the order of the grain size so dislocations emitted from one boundary would be absorbed into an adjacent boundary leading to little increase in dislocation density.

Our current observations suggest that rolling of the Al-1.2C-0.90 alloy does not work harden the material and annealing at temperatures up to 630°C allows little recovery. This is to be expected from the high dispersoid drag pressure in this alloy. However, superplastic properties of this type of material indicate that structural evolution can occur during concurrent annealing and deformation for various strain rates, so our efforts are now focused on this topic.

4. Future Activities

The gradual changes that lead to the formation of medium-angle boundaries in Al-.24Zr-0.1Si will be studied with transmission microscopy and possibly also differential scanning calorimetry. The effect of strain-rate on the deformation behavior and microstructure during elevated temperature straining will be studied with transmission microscopy and compared to the static recrystallization behavior. The same kind of elevated deformation studies will be done on Al-1.2C-0.90 for a wide range of strain rates. These observations will form the basis for a model of the recovery and continuous recrystallization behavior of materials having a wide range of dispersoid drag pressures.

During preparation of this report, new observations of superplastic-like behavior at high strain rates were reported by Bieler and coworkers [42] for MA aluminum alloys similar to those

being investigated within the subject contract. These workers report obtaining elongations in excess of 500% at strain rates near 10 s^{-1} . This strain rate is approximately 10^4 faster than strain rates normally associated with superplastic behavior, and corresponds to a reduction of component forming time from hours to seconds. This exciting breakthrough has the potential to shift superplastic forming from a slow process suited to production of aerospace components at a rate of several per day to a fabrication method with broad application to many defense and commercial products.

The mechanisms that provide the superplastic-like behavior at high strain rates appear to be similar to those associated with superplasticity at conventional rates. The finer grain size of the MA material is thought to shift superplastic behavior to high strain rates. Thus, the mechanism responsible for superplastic-like behavior is at least tentatively identified, but the functions of the various thermomechanical processing steps used to produce material that exhibits this behavior are essentially unknown. For example,

- Can other alloys be processed to obtain similar behavior?
- Must these alloys be mechanically-alloyed, or can they be processed by PM or conventional methods?
- Is the stress state during deformation critical?

The answers to these questions remain open, but the course of investigation being pursued in the present study is designed to provide answers to several of these basic questions.

5. References

1. H. Alborn, E. Hornbogen and U. Koster, *J. Mat. Sci.*, 4 (1969) 944-950.
2. J.W. Martin and R.D. Doherty, Stability of Microstructure in Metallic Systems, Cambridge University Press, Cambridge, 1976, pp. 150-153.
3. E. Nes, "Continuous Recrystallization and Grain Growth during Superplastic Flow", in Superplasticite/Superplasticity, B. Baudalet and M. Suery (eds.), Editions du CNRS, Paris, 1985, pp. 7.1-7.11.
4. T.R. McNelley, E.-W. Lee and M.E. Mills, *Met. Trans.*, 17A (1986) 1035-1041.
5. E.-W. Lee, T.R. McNelley, A.E. Stengel, *Met. Trans.*, 17A (1986) 1043-1050.
6. J.P. Hirth, *Met. Trans.*, 3 (1972) 3047-3067.
7. S.P. Agrawal (ed), Superplastic Forming, American Society for Metals, Metals Park, 1985.
8. D.J. Lloyd, *Metal Science*, 14 (1980) 193-198.
9. J.A. Wert, "Thermomechanical Processing of Heat-Treatable Aluminum Alloys for Grain Size Control," in Microstructural Control in Aluminum Alloys, E.H. Chia and H.J. McQueen (eds.), The Metallurgical Society of AIME, Warrendale, PA, 1986, pp. 67-94.
10. F.J. Humphreys, *Acta Met.*, 25 (1978) 1323-1344.
11. F.J. Humphreys, *Metal Science*, 13 (1979) 136-145.
12. F.J. Humphreys, "Nucleation of Recrystallization in Metals and Alloys," 1st Riso Int. Symp. on Metallurgy and Materials

Science, Roskilde, Denmark, 1980, pp. 35-44.

13. R. Sandstrom, "Criteria for Nucleation of Recrystallization Around Particles," 1st Riso Int. Symp. on Metallurgy and Materials Science, Roskilde, Denmark, 1980, pp. 45-49.

14. R. Sandstrom, Z. Metallkde., 71 (1980) 681-688.

15. R.D. Doherty, "Nucleation of Recrystallization in Single Phase and Dispersion Hardened Polycrystalline Materials," 1st Riso Int. Symp. on Metallurgy and Materials Science, Roskilde, Denmark, 1980, pp. 57-69.

16. C.S. Smith, Trans AIME, 175 (1948) 15-48.

17. M.F. Ashby, J. Harper and J. Lewis, Trans AIME, 245 (1969) 413-420.

18. C.J. Tweed, B. Ralph and N. Hansen, Acta Met., 32 (1984) 1407-1414.

19. E. Nes, N. Ryum and O. Hunderi, Acta Met., 33 (1985) 11-22.

20. J.A. Wert, N.E. Paton, C.H. Hamilton and M.W. Mahoney, Met. Trans., 12A (1981) 1267-1276.

21. R.D. Doherty, Metal Science, 8 (1974) 132-142.

22. B. Bay and N. Hansen, Met. Trans., 10A (1978) 279-288.

23. N.E. Paton, J.A. Wert and J.C. Chesnutt, Final Report, AFOSR Contract F44620-76-C-0025, March 1980.

24. E. Nes, Scripta Met., 10 (1976) 1025-1028.

25. E. Nes, Acta Met., 24 (1976) 391-398.

26. E. Nes, "Grain Size and Texture Control in Commercial Aluminum Alloys," Proc. 7th Int. Light Metals Congress, Leoben/Vienna, 1981, pp. 154-155.

27. R. Sandstrom, Z. Metallkde., 71 (1980) 741-751.

28. E. Nes and S. Slevden, Aluminium, 55 (1979) 319-324.
29. E. Nes, Metalurgia I. Odlwunictwo, 5 (1979) 209-224.
30. E. Nes, "Recrystallization in Alloys with Bimodal Particle Size Distributions," in Proc. 1st Riso Int. on Metallurgy and Materials Science, Roskilde, Denmark, 1980, pp. 85-95.
31. E. Nes and J.A. Wert, Scripta Met., 18 (1984) 1433-1438.
32. J.A. Wert and L.K. Austin, Met Trans., in press.
33. B.M. Watts, M.J. Stowell, B.L. Baikie and D.G.E. Owen, Metal Science, 10 (1976) 189-197.
34. B.M. Watts, M.J. Stowell, B.L. Baikie and D.G.E. Owen, Metal Science, 10 (1976) 198-206.
35. R. Grimes, M.J. Stowell and B.M. Watts, Metals Technology, 3 (1976) 154-160.
36. O. Reiso, H. Westengen, L. Auran, 7th Light Metals Congress, Leoben, Vienna, (1981) 186-188.
37. P.S. Gilman, W.D. Nix, Met. Trans., 12, (1981), 813-824.
38. R.T. Chen, E.A. Starke, Jr., Techn. Paper 8408-034, 1984 ASM Metals Congress, Detroit, Michigan, (1984).
39. E. Nes, Metal Science, 13, (1979), 211-215.
40. E. Nes, H. Billdal, Acta. Met., 25, (1977), 1039-1046.
41. Y.-W. Kim, L.R. Bidwell, Scripta Met., 15, (1981), 483-486.
42. T.R. Bieler, T.G. Nieh, J. Wadsworth and A.K. Mukherjee, Scripta Met., 22 (1988) 81-86.

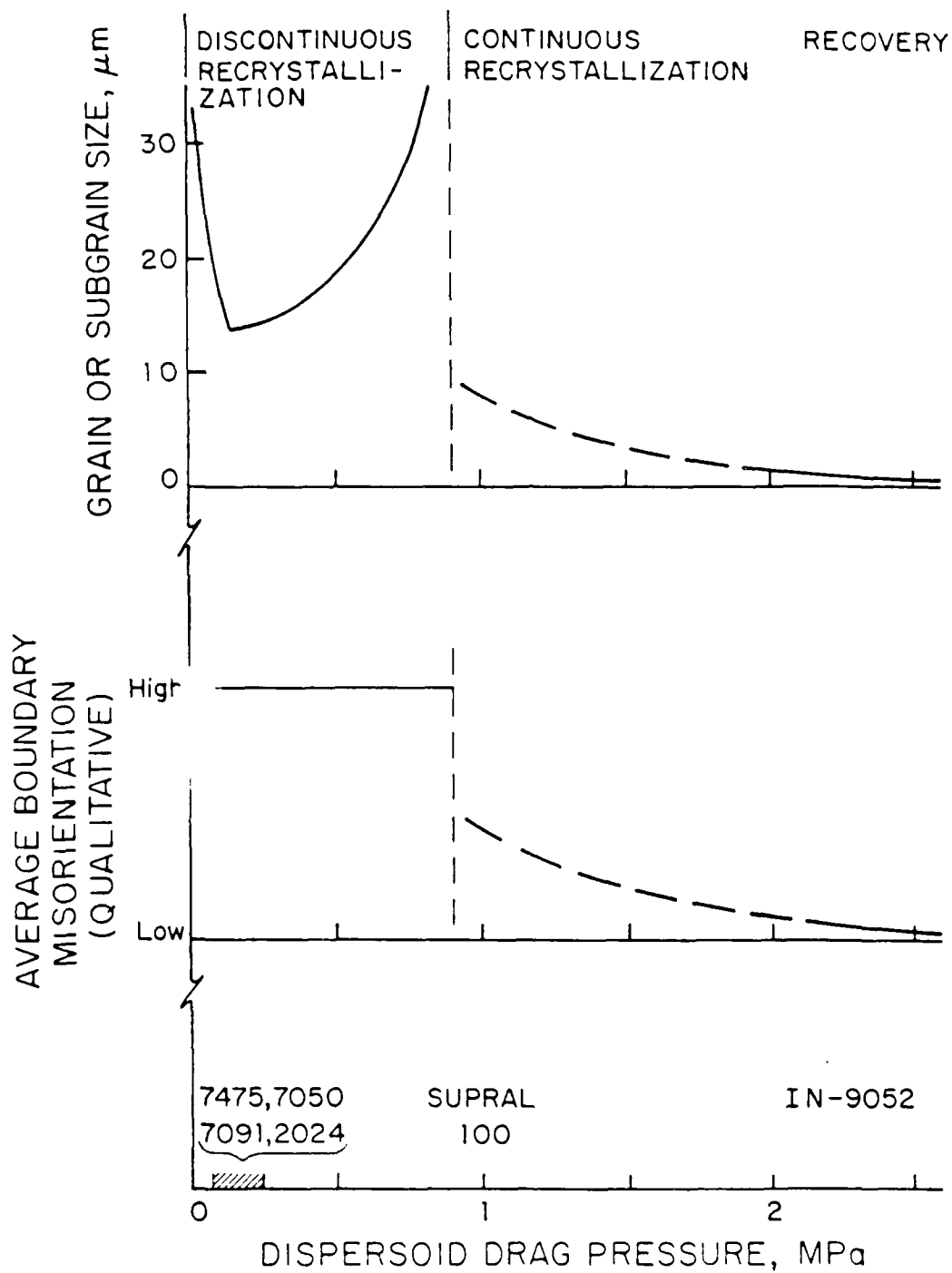
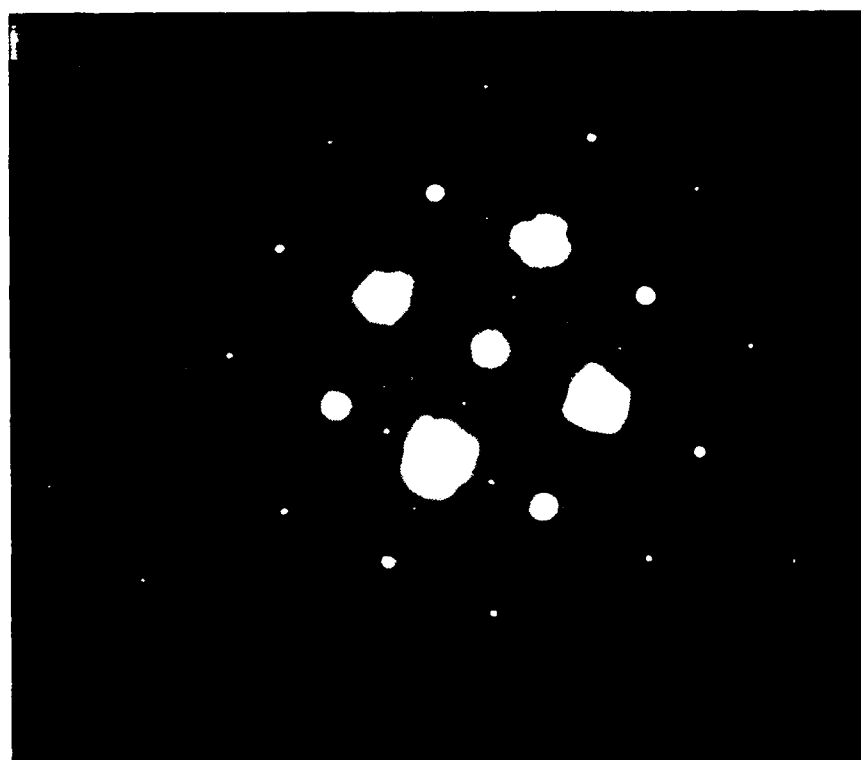


Fig. 1 (a) Grain size as a function of dispersoid particle drag pressure. (b) Grain boundary misorientation as a function of dispersoid drag pressure. (c) Approximate positions of several aluminum alloys on dispersoid particle drag pressure axis.



A



B

Fig. 2 (a) Dark field image of precipitated Al₃Zr particles in Al-0.26Zr-0.1Si after annealing for 8 hrs. at 450°C, heating rate 50°C/hr. (b) SAD pattern showing the [001] zone axis of the coherent simple cubic Al₃Zr phase. Lattice parameter 0.405 nm.

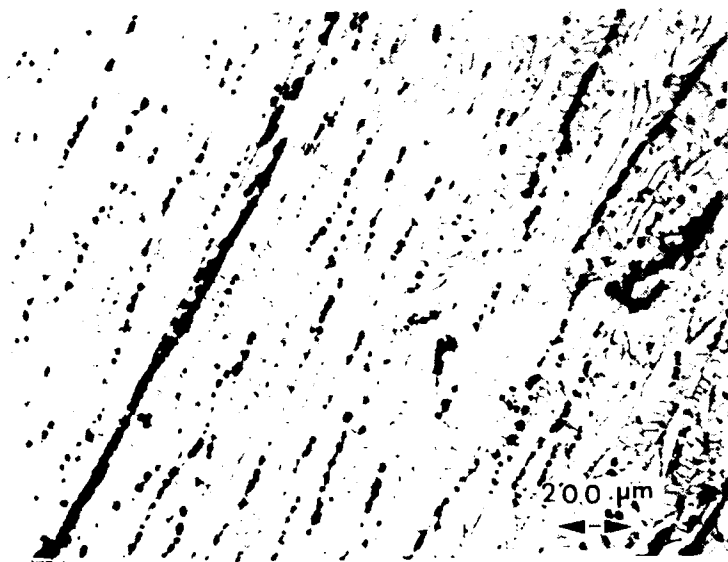


Fig. 3 Segregation of Zr in a section from the chill-zone of a direct chill cast ingot. The light regions are Zr rich. Al-0.26Zr-0.1Si, etched in 10% NaOH solution for 4 minutes at 65°C.

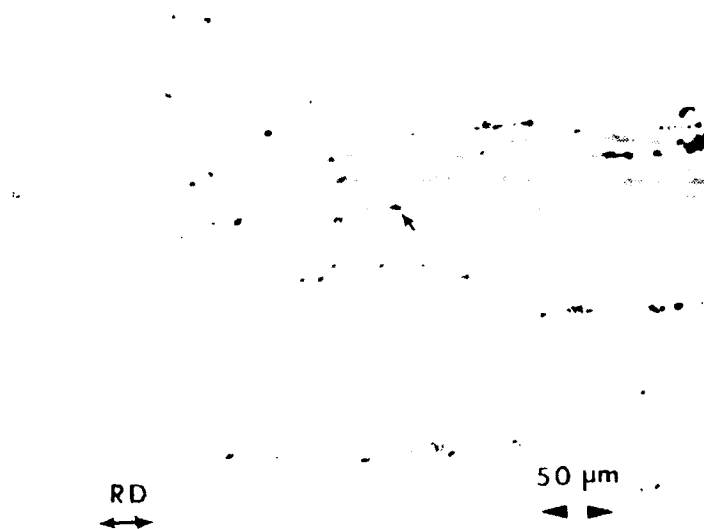


Fig. 4 Coarse primary Al_3Zr particles in the chill zone of a direct chill cast Al-0.46%Zr-0.1Si ingot. Barker's etch.

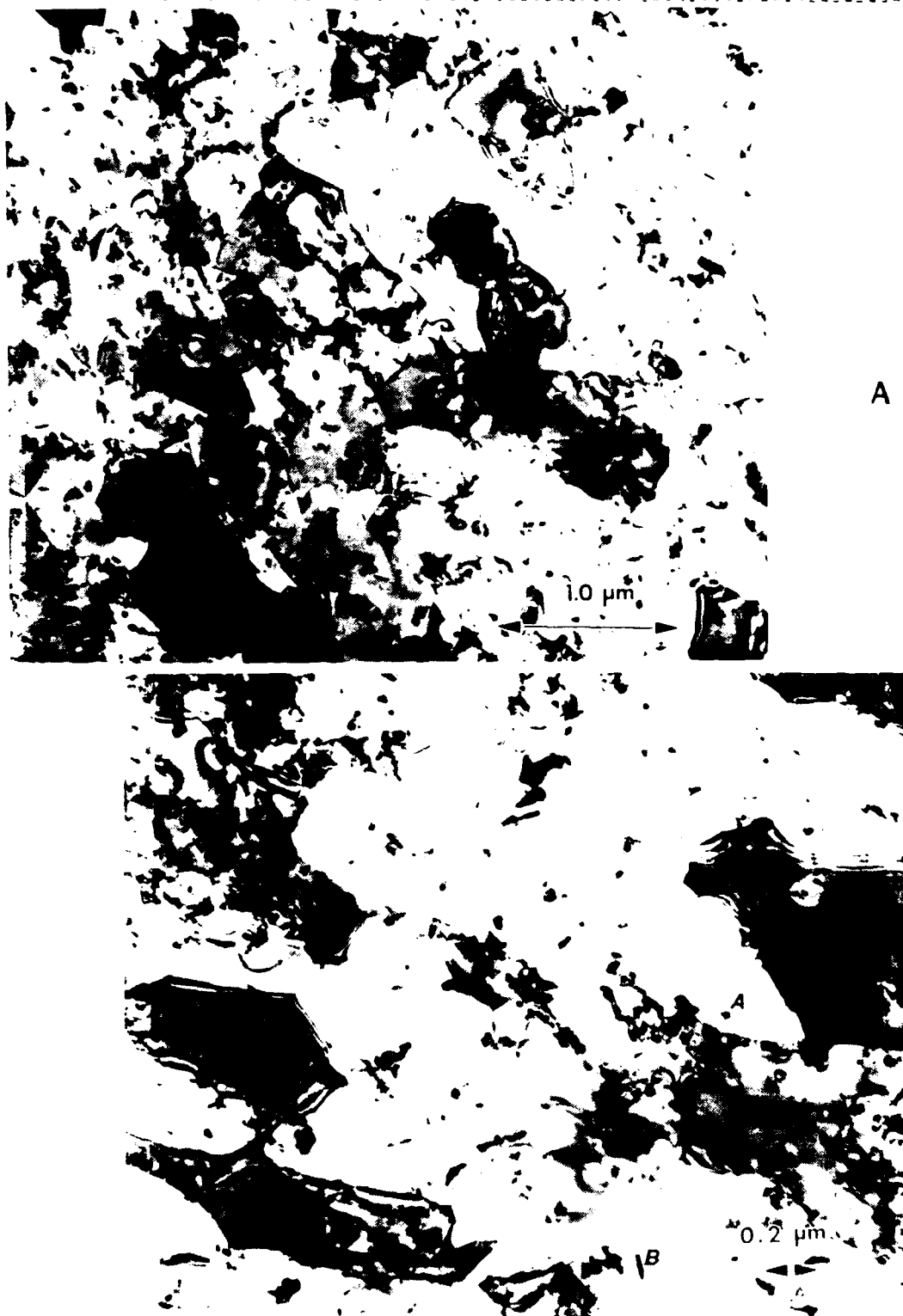


Fig. 5 (a) Bright field image of the microstructure in Al-1.2C-0.90 after an 8 hour anneal at 600°C. (b) Dispersoids in the same material. (Transverse sections)

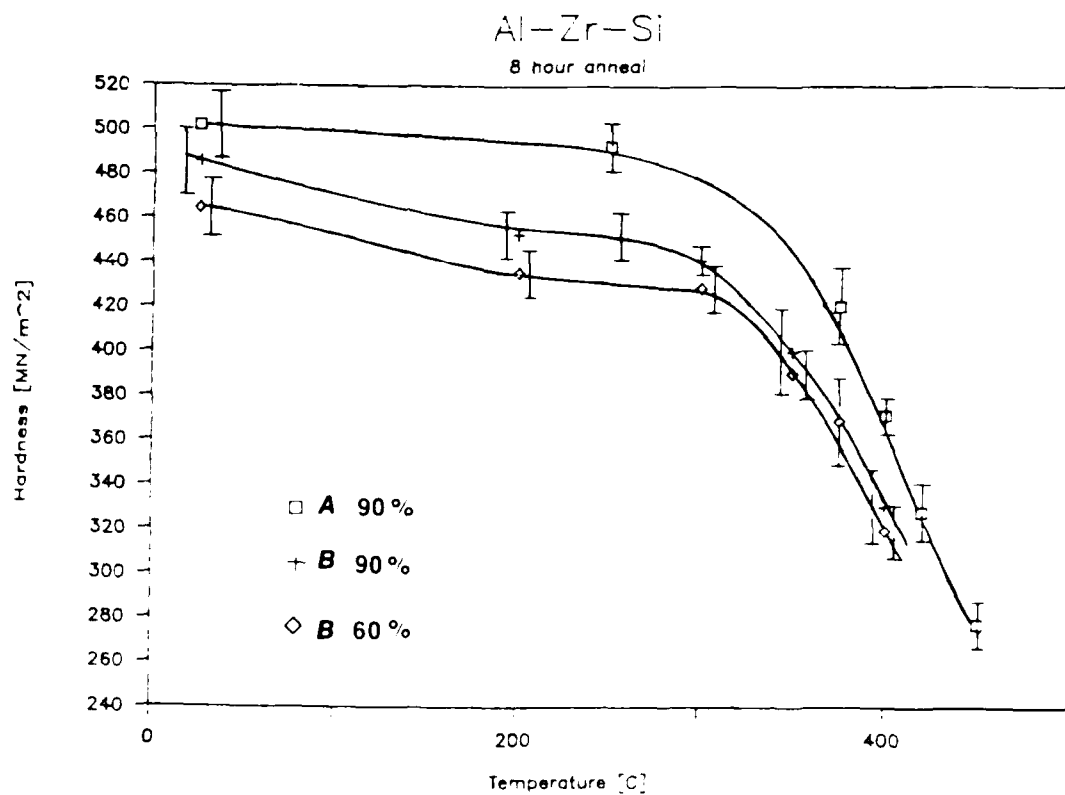


Fig. 6 Hardness as a function of annealing temperature (8 hr anneal). Material A: 0.8kg/30 sec, as heat treated hardness = 296 ± 15 MN/m². Material B, 90% reduction: 0.8kg/30 sec, as heat treated hardness = 247 ± 7 MN/m². Material B, 60% reduction: 2kg/30 sec, as heat treated hardness = 247 ± 7 MN/m².

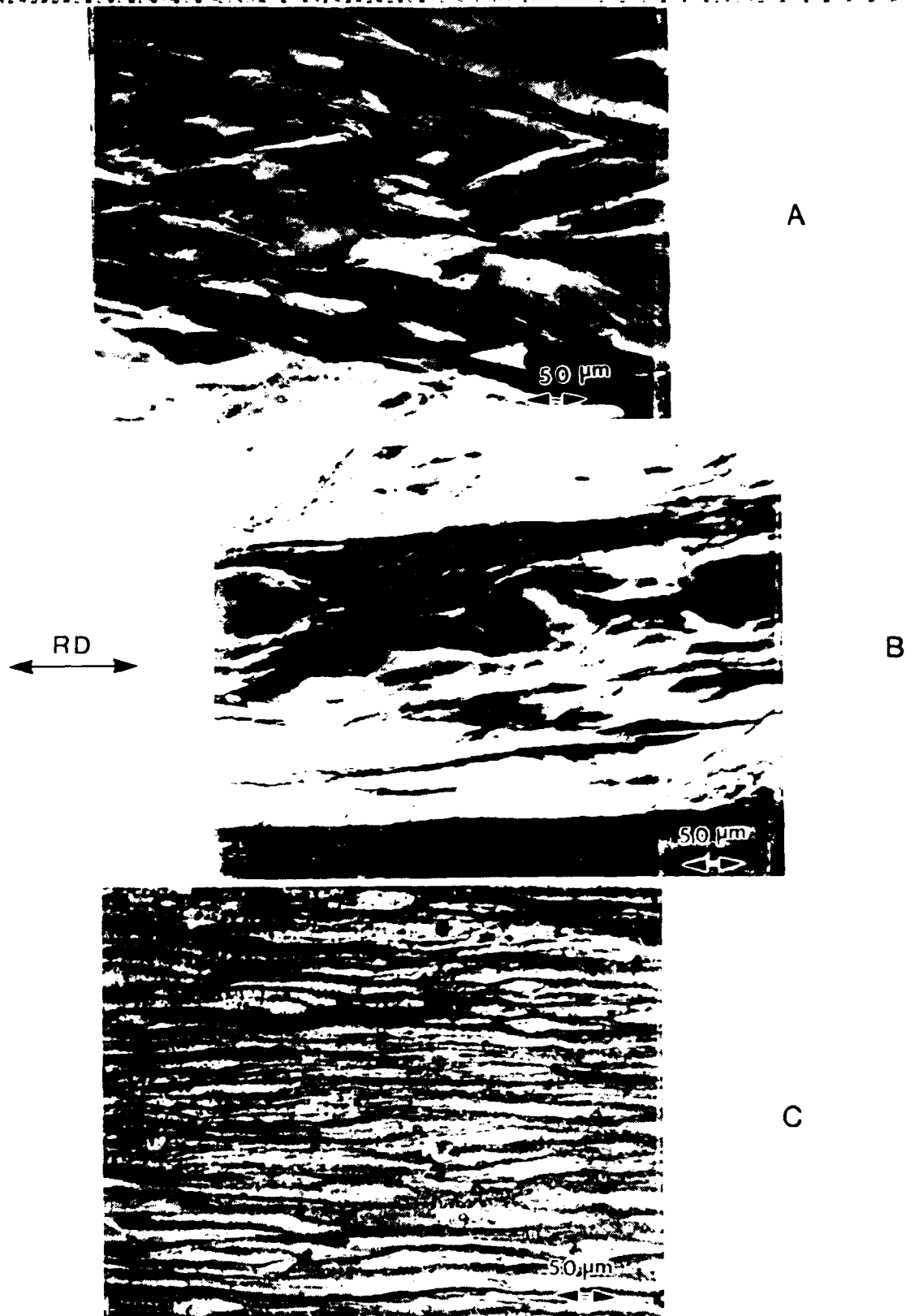


Fig. 7 (a) Material B (60% reduction) as rolled, "hard island" arrowed. (Transverse section, Barkers etch) (b) Material B (75% reduction) as rolled. (Transverse section, 10% NaOH etch) (c) Material A (90% reduction) as rolled. (Transverse section, 10% NaOH etch)



A




B



Fig. 8 (a) Bright field image of Zr rich area surrounded by deformation cells. Note the microband formation in the Zr rich area. (b) Bright field image of the sharp boundary between regions of different Al_3Zr density. (Transverse sections)



A

100um

 RD

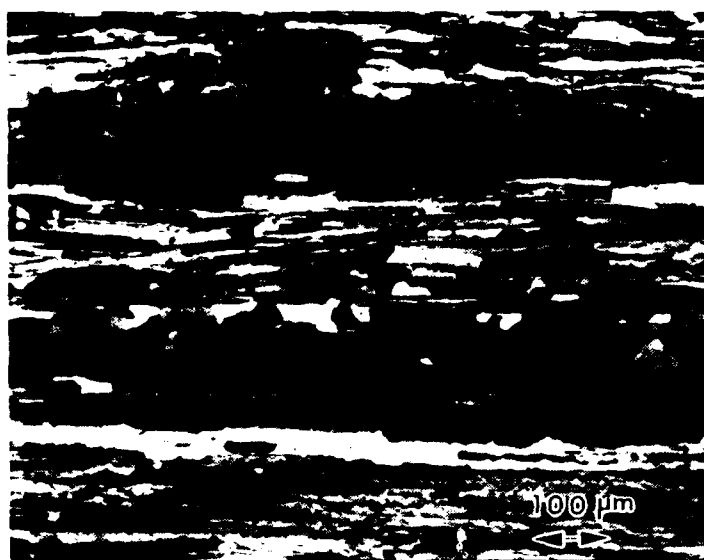


B

Fig. 9 (a) Material B (75% reduction, 350°C/8 hours)
 (b) Material B (90% reduction, 350°C/8 hours)
 (Barkes etch, transverse sections)



A



B

Fig. 10 (a) Material A (90% reduction, 400°C/8 hours)
 (b) Material B (90% reduction, 400°C/8 hours)
 (Barkers etch, transverse sections)

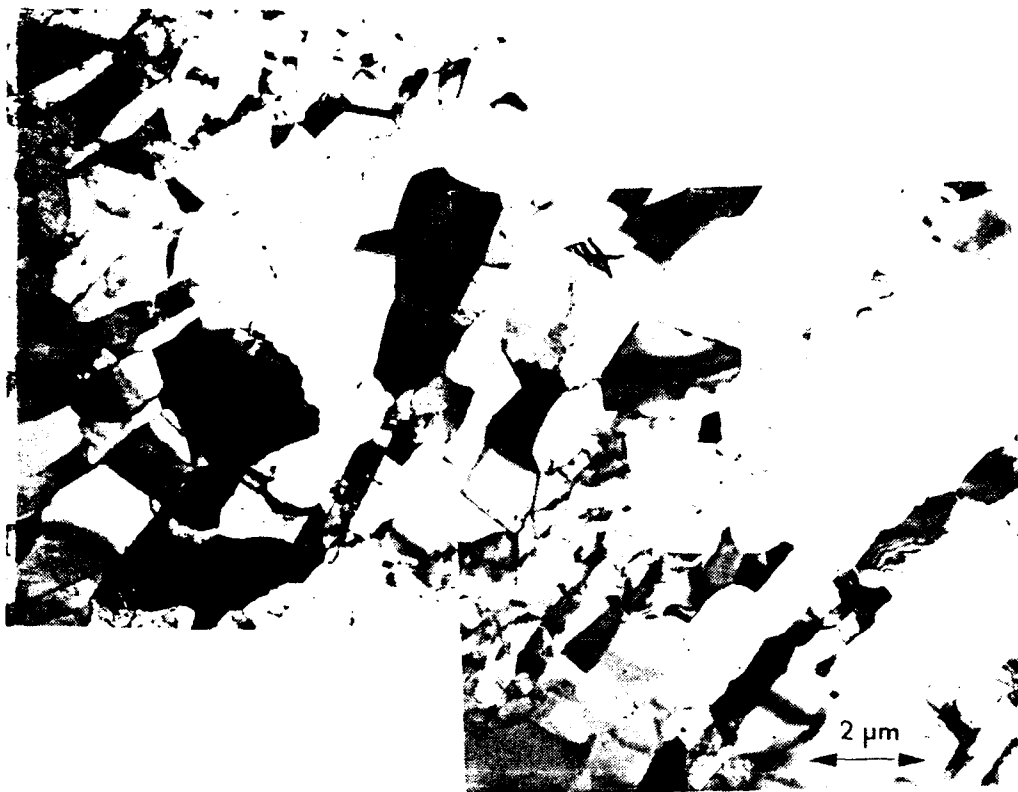
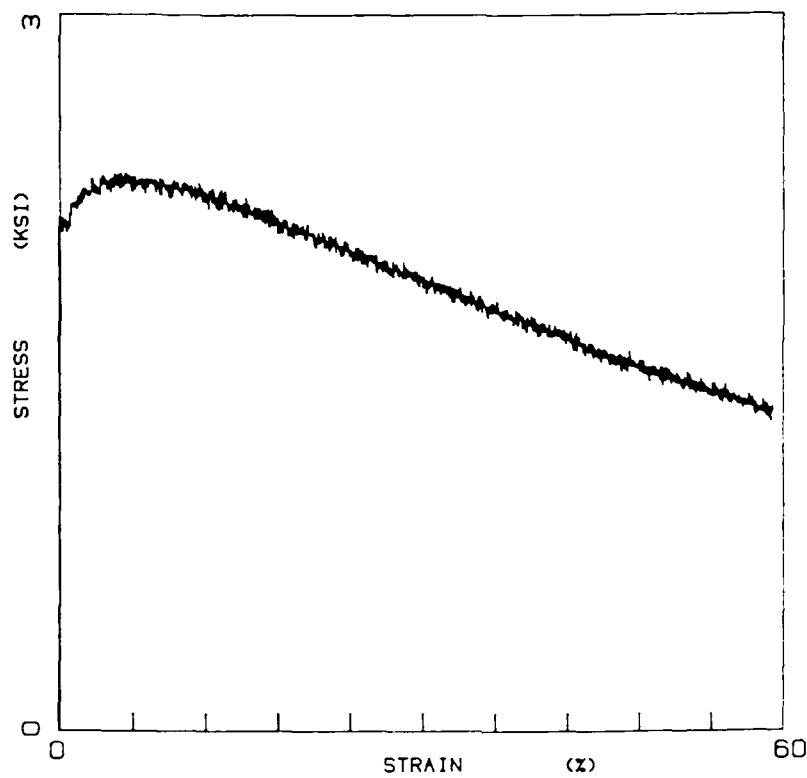


Fig. 11 Bright field images of the microstructure of material A, 90% reduction, 400°C/ 8 hours. (Transverse sections)



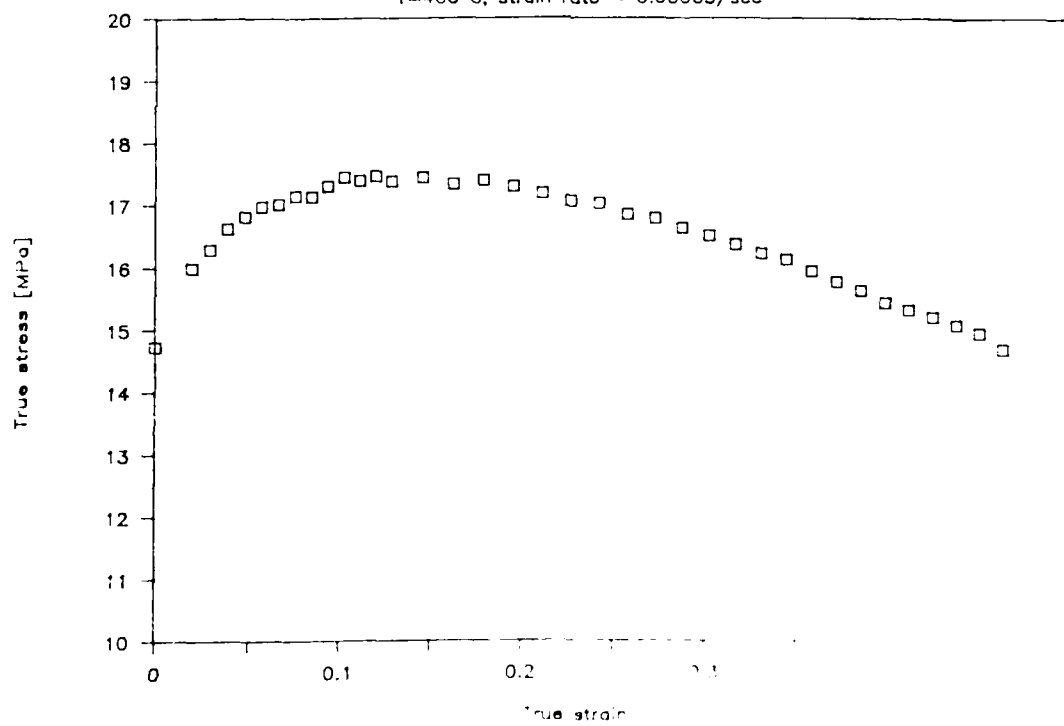
Fig. 12 Bright field montage of the microstructure of material A, 90% reduction, 400°C/8 hours. The numbers indicate the misorientation angle between the grains. (Transverse section)



A

Al-0.1%Si-0.24%Zr

T=400 C, strain rate = 0.00065/sec



B

Fig. 13 (a) Engineering stress-engineering strain for material A, as rolled 90%, T = 400 C, strain rate = 0.00065/sec
(b) True stress-true strain for material A

AD-A193 224

PROCESSING AND PROPERTIES OF ADVANCED ALUMINUM ALLOYS

2/2

(U) VIRGINIA UNIV CHARLOTTESVILLE DEPT OF MATERIALS

SCIENCE J A WERT ET AL. FEB 88 UVA/525670/MS88/101

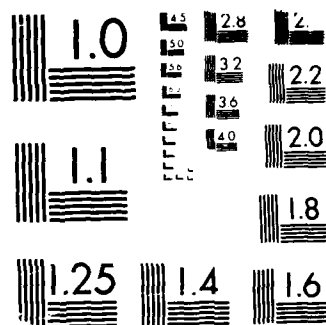
UNCLASSIFIED

AFOSR-TR-88-0285 AFOSR-87-0082

F/G 11/6.1

NL

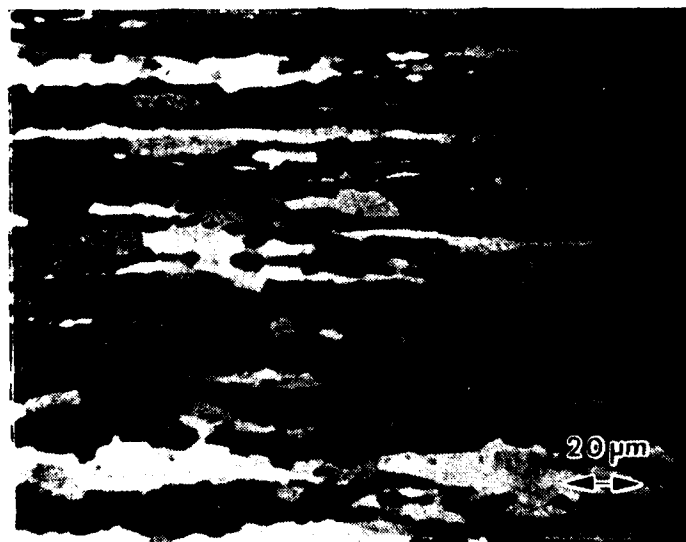




MICROCOPY RESOLUTION TEST CHART



A



B

Fig. 14 (a) and (b) Microstructure in gauge section for the same material as in Fig. 13. (Transverse sections)

DISTRIBUTION LIST

Copy No.

1 - 6	Air Force Office of Scientific Research/NE Building 410 Bolling Air Force Base Washington, D.C. 20332 Attention: Dr. Alan H. Rosenstein
7 - 8	J. A. Wert, MS
9 - 10	E. A. Starke, Jr., MS
11	T. H. Courtney, MS
12 - 13	E. H. Pancake, Clark Hall
14	SEAS Publications Files

JO#1061:jl b

UNIVERSITY OF VIRGINIA
School of Engineering and Applied Science

The University of Virginia's School of Engineering and Applied Science has an undergraduate enrollment of approximately 1,500 students with a graduate enrollment of approximately 560. There are 150 faculty members, a majority of whom conduct research in addition to teaching.

Research is a vital part of the educational program and interests parallel academic specialties. These range from the classical engineering disciplines of Chemical, Civil, Electrical, and Mechanical and Aerospace to newer, more specialized fields of Biomedical Engineering, Systems Engineering, Materials Science, Nuclear Engineering and Engineering Physics, Applied Mathematics and Computer Science. Within these disciplines there are well equipped laboratories for conducting highly specialized research. All departments offer the doctorate; Biomedical and Materials Science grant only graduate degrees. In addition, courses in the humanities are offered within the School.

The University of Virginia (which includes approximately 2,000 faculty and a total of full-time student enrollment of about 16,400), also offers professional degrees under the schools of Architecture, Law, Medicine, Nursing, Commerce, Business Administration, and Education. In addition, the College of Arts and Sciences houses departments of Mathematics, Physics, Chemistry and others relevant to the engineering research program. The School of Engineering and Applied Science is an integral part of this University community which provides opportunities for interdisciplinary work in pursuit of the basic goals of education, research, and public service.

END

DATE

FILMED

DTIC

JULY 88